An Analysis of Surface Area Estimates of Binary Volumes Under Three Tilings

by

Erik G. Miller

Submitted to the Department of Electrical Engineering and Computer Science
in partial fulfillment of the requirements for the degree of

Master of Science in Electrical Engineering

at the

MASSACHUSETTS INSTITUTE OF TECHNOLOGY

June 1997

Author .....
Department of Electrical Engineering and Computer Science
May 18, 1997

Certified by .....
Berthold K. P. Horn
Professor of Electrical Engineering and Computer Science
Thesis Supervisor

Accepted by .....
Arthur C. Smith
Chairman, Departmental Committee on Graduate Students

An Analysis of Surface Area Estimates of Binary Volumes Under Three Tilings

by

Erik G. Miller

Submitted to the Department of Electrical Engineering and Computer Science
on May 18, 1997, in partial fulfillment of the
requirements for the degree of
Master of Science in Electrical Engineering

Abstract

In this paper, we first review local counting methods for perimeter estimation of piecewise smooth binary figures on square and hexagonal grids. We verify that better perimeter estimates can be obtained on a hexagonal grid. We then compare surface area estimates using local counting techniques for binary three-dimensional volumes under three distinct tilings: the cubic, truncated octahedral, and rhombic dodecahedral tilings. It is shown that under certain assumptions of piecewise smoothness, the mean error of surface area estimates is smaller for the truncated octahedral and rhombic dodecahedral tilings than for the standard cubic or rectangular prism tilings of space. Additional properties of these tessellations are reviewed and potential applications of better surface area estimates are discussed.

Thesis Supervisor: Berthold K. P. Horn
Title: Professor of Electrical Engineering and Computer Science

Acknowledgments

It was an honor and a pleasure to work with Professor Berthold K. P. Horn on this project. His enthusiasm and support for the "basic research" presented here was a great motivating force. I was most grateful for his willingness to discuss the abstruse and obscure details of this project at a moment's notice.

I thank in particular Chris Stauffer for several "breakthrough" discussions and ideas about 3-D geometry, without which I may not have been able to turn this work into a thesis. I have a debt to Oded Maron and to Carl de Marcken for actually reading an entire draft and making helpful suggestions.

I also thank Polina Golland, Jeremy De Bonet, and Greg Galperin for helpful discussions related to this work.

I would like to thank Professor Paul Viola for his support during this project and for his patience in my completion of it. Professor Eric Grimson has also been pivotal in providing a supportive and relaxed atmosphere during my first two years at MIT.

Contents

List of Figures

List of Tables

Chapter 1

Introduction

To represent images or volumes in a digital computer, they must be discretized. This discretization leads to errors in the computation of such fundamental properties of objects as perimeter, area, volume, and surface area. Not surprisingly, the magnitudes of these errors depend upon the particular discretization used. There are an infinite variety of discrete approximations for any planar figure, from the spatial frequency decompositions used in signal processing to parameterized NURB surfaces used in the CAD/CAM world. In this thesis, we focus on a particular class of discretizations: the *tessellation* of planar figures and solid volumes. Tessellations are approximate representations particularly convenient in computer vision and graphics.

1.1 Some Definitions

We define the *tessellation of a figure* (in either two or three dimensions) as the discretization of the figure into a finite number of continuous regions, each having a constant value (See Figure 1-1). The value of each region is some measure of the original figure in that vicinity, such as a point sample of the figure at the centroid of the region or a spatial average over the region. In two dimensions, these regions are typically dubbed *pixels*, for picture elements, and in three dimensions *voxels*, for volume elements. In this thesis, we use the term *tiling* synonymously with tessellation, and each element of a tessellation is sometimes referred to as a *tile*, especially if the

dimension is unspecified. The term *grid* shall be used to denote the specific arrangement of tiles used to cover a space. For example, squares can be placed in the common Cartesian grid (like ordinary graph paper), or can be arranged so that each row is offset by some distance from the previous row (as in a brick wall). When discussing a tiling by a particular tile which has more than one possible associated grid (only the square and cubic grids in this paper), it will be assumed unless stated otherwise that the Cartesian grid is intended. Tiling a figure on a Cartesian square or rectangular grid (such as that of a typical raster display) is frequently called *rasterization* [4].

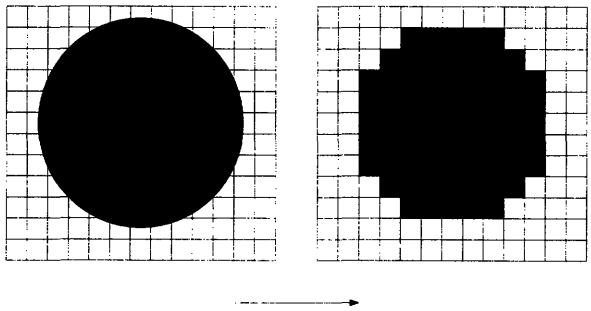

Figure 1-1: The tessellation of a circle on a square grid. Here, the original figure was sampled at the center of each tile, and this value was copied across the whole tile. The figure on the left is a *continuous binary image.* The figure on the right is a *discrete binary image.*

In the following analyses, we restrict our focus to *binary* images and volumes, i.e. data sets in which each pixel or voxel has one of two values (black or white, 0 or 1, etc.). Much of the previous work on properties of tessellations does the same: [2, 6, 7, 9]. Prior to tessellation we call a binary image *continuous.* After tessellation, it becomes a *discrete* binary image. The same terminology applies to volumes.

1.2 Local Counting Algorithms

Much of the work in discrete binary image processing has focused on *local counting algorithms* [7, 11]. These techniques involve computing functions of figures when only local image information is available for computations, and local results are reported to a global accumulator. For example, in a black and white image, the perimeter of a tessellated figure can be computed using a local counting scheme as follows: a

processor at each black pixel reports to the global accumulator the length of its border with neighboring white pixels. The sum of the results from each processor is the exact perimeter of the tessellated figure. It is also a *perimeter estimate* (not always a good one!) of the originally imaged object from which the tessellated figure was derived. Local counting algorithms have been motivated in part by their inherent parallelism and simplicity of implementation, making them ideal for use on fine grain, highly parallel computers.

In two dimensions, there are three common functions which can be computed using local counting schemes: area, perimeter, and Euler number (a topological measure equal to the number of objects in an image less the number of holes). All of these functions obey the *additive set property* [9], the condition which allows the individual local measures to be combined into a global measure. Local counting algorithms produce exact results for these three functions on tessellated figures. However, if we use the value of a function computed for a tessellated figure as an estimate of the value of that function for the figure from which it came, we may get significant errors. And as we shall see, the error behavior of these algorithms varies significantly under different tessellations. We shall also see that while increasing the resolution of our grid can give us arbitrarily good measures of both Euler number and area, this is not the case for perimeter measures.

1.2.1 Exact Euler Number Computation

A figure's Euler number is by definition an integer, and it can be computed exactly even after a figure has been discretized provided that the discretization of the figure did not alter its topology in any way. If we make the tessellation too coarse, we will begin to lose information about the figure's topology. While for certain figures, one may be able to maintain the correct Euler number using a coarser hexagonal tessellation than with a similar resolution square tessellation, we can be sure that we can perfectly represent Euler number with some finite sized tessellation for either grid. That is, for all smooth figures f with well defined Euler numbers,

$$\exists n < \infty : E'_n(f) = E(f), \tag{1.1}$$

where E is the original figure's Euler number and E'_n is the estimate of E on a grid with n pixels of a particular shape.

In Figure 1-2, we are unable to represent the Euler number of a continuous "V-shaped" region unambiguously with a coarse square tessellation (A). This is not an adequate representation since it is not clear whether we have one or three "holes" in the middle of the figure. A finer square tessellation (B), however, does the job. Here, we can unambiguously determine the true topology of the original figure. In (C), we were able to achieve this same result with a coarse hexagonal grid, although it is not true in general that a hexagonal grid will be able to represent exact Euler number with fewer pixels.[1]

The main point, however, as summarized in Equation 1.1 is that we can always compute Euler number exactly by choosing a small enough grid, regardless of the *shape* of the pixels we use. This condition does not hold for other measures computed with local counting schemes.

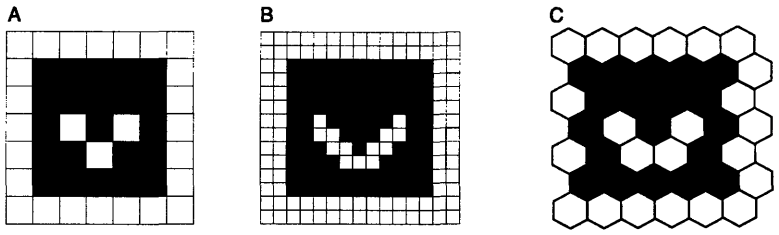

Figure 1-2: Euler number on various grids. **A.** Here, it is not clear whether the figure has one, two, or three holes. **B.** Increasing the resolution enough will always solve the problem. **C.** Sometimes, but not always, the hexagonal grid provides a more efficient representation of a figure while preserving the original Euler number.

[1] Horn [9] points out that Euler number on a hexagonal grid is never ambiguous since there is no ambiguity in the definition of adjacency. The Euler number on a square grid can be ambiguous since it is not clear whether two pixels touching by a corner are adjacent [2, 6]. However, this does not in general mean that we can represent the true topology of a figure more efficiently on a hexagonal grid. The verity of this conjecture is not addressed here.

1.2.2 Arbitrarily Accurate Area Computation

In particular, we cannot recover the exact area of a figure after it has been tessellated. It is not hard to see that for common figures with piecewise smooth borders, that the expected magnitude of the relative error in the computation of area is related to the ratio of the number of pixels which intersect the figure's border to the number of pixels completely contained within the figure. For plane figures whose borders are piecewise smooth and continuous, this ratio approaches zero as the area of each pixel goes to zero. That is:

$$\lim_{n\to\infty} A'_n(f) = A(f), \tag{1.2}$$

where f is again a piecewise smooth figure, n is the number of pixels used to represent the figure, and $A'_n(f)$ is the approximate area based on a local counting algorithm for area computation, and $A(f)$ is the true area of the figure. This result holds for all convex tessellations. While different tessellations may give better results for a certain number of pixels, we can obtain an error as small as we like by choosing small enough pixels, regardless of the shape of the pixels.

1.2.3 Accurate Perimeter Computation?

While Euler number and area can be approximated with arbitrary accuracy by merely increasing the resolution of our grid, the estimation of perimeter presents a special problem. Before embarking on an analysis of perimeter, however, we make the following simplification.

Random Line Segment Length Estimation as a Substitute for Random Plane Figure Perimeter Estimation

We want to show, in an informal way, that certain statistics of random figure processes will have the same value as the equivalent statistics for random line processes. If we can do this, we have simplified our analysis of perimeter estimate to one of line segment length estimates. This will depend upon restricting the class of figures we are analyzing as well as making certain assumptions about the meaning of "random".

We note that each member of the set of simple, closed, piecewise smooth, planar curves can be "closely" approximated by a finite number of constant length line segments. Figure 1-3 illustrates this idea. If we choose a large enough number of

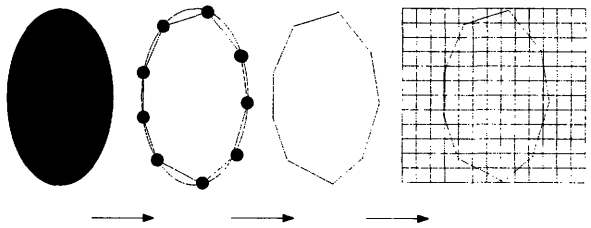

Figure 1-3: The approximation of a boundary with a finite number of fixed-length line segments. By representing a boundary as piecewise linear, we greatly simplify the analysis of the boundary's behavior under various tessellations.

segments with which to approximate a curve, then each segment of the curve will be arbitrarily well approximated by a line segment. The perimeter of this approximation can be made arbitrarily close to the true perimeter of the figure, which is achieved in the limit when the length of each segment goes to zero and the number of segments goes to infinity. Such a construction follows the reasoning in the derivation of the integral of arc length along the curve.

Now we are interested in the estimation of perimeter for "arbitrary" or "random" planar figures, since we wish to examine the expected values of various functions of estimated perimeter for any figure we may encounter. We choose to define *random* piecewise smooth planar curves so that figures of any orientation and position are equally probable. That is, we define random so that if a figure F has probability density P, then an arbitrary rotation and translation of that figure F' also has probability density P. For the purposes of this paper, we do not need to further restrict our notion of random, since we are only interested in showing that border segments of any orientation are equally probably. For example, it is of no concern to us whether a large piecewise smooth planar figure is more or less probable than a smaller piecewise smooth planar figure, since approximations to both (over all of their possible orientations) will contribute equally to the uniform distribution of line segment orientations in our analysis. To use the terminology of stochastic geometry, we are restricting our *density* of random piecewise smooth simple closed curves to

be *invariant to the choice of coordinate system*, a common approach when discussing geometric stochastic processes [23].

If curves of any rotation are equally probable then we can choose finite line segment approximations to those curves in such a way that the orientation of the line segments (relative to the x-axis) is also evenly distributed. That is, we are interpreting "random figures" to be well approximated by collections of "random line segments". Hence, the perimeter of these random curves can be estimated in the same way as the length of random line segments. In this way, we reduce the problem of the analysis of random curves to the analysis of random line segments, a considerable simplification.

City Block Distance

We now address the problem of estimating the length of a line segment (and hence a piecewise smooth curve) on a finite grid. Figure 1-4 shows the basic approach to estimating the length of a line segment using the so called *city block distance* [15]. This figure represents the worst case scenario in which we overestimate the length of the line by a factor of $\sqrt{2} \approx 1.414$. We again ask the question of whether increasing the resolution of the grid will improve the estimate. The answer is that up to a certain point, increasing the resolution will improve perimeter estimates, but that beyond a certain resolution, we will not be able to significantly reduce the perimeter error by increasing the resolution.

Below, we examine the reasons for this statement. Consider a polygon represented on two grids of differing resolution, as in Figures 1-5A and 1-5B.

Case 1: Improved resolution DOES improve perimeter estimate

If we estimate the perimeter of this polygon between points X and Z in these figures, we will obtain different results for the two grids because the pixels in Figure 1-5A are too large to adequately represent the polygon, while those in Figure 1-5B capture most of the variation in the shape. For this particular measurement, we would obtain a more accurate result on the grid in Figure 1-5B. To simplify the analysis in this paper, we assume that the pixel size is small enough so that errors of this type will be

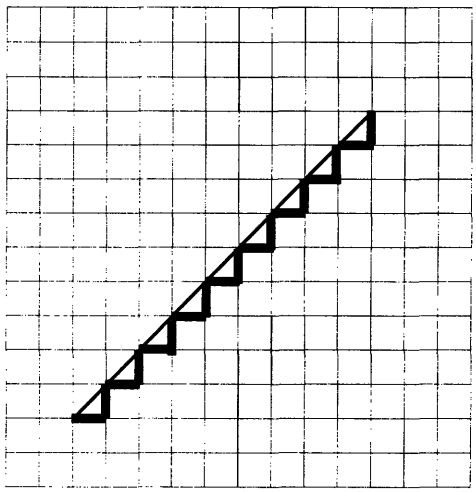

Figure 1-4: Estimating line length using *city block distance.* Each pixel through which the line passes computes its contribution to length, marked by the heavy dark segments. It reports these lengths to a global accumulator, which estimates the total length of the line segment.

insignificant. For this to be true, it is necessary that the number of non-differentiable points in the piecewise smooth curve be small relative to the number of pixels that the curve passes through. The exact ratio of these quantities is determined by the accuracy we are trying to achieve. But the errors due to this phenomenon can be made as small as desired by choosing a high enough resolution for the grid. (It should be pointed out that the analyses which follow in this paper have no bearing on curves which are not piecewise smooth, such as fractal curves like the border of the Mandelbrot Set.) However, even when figures are smooth enough and the tessellating grid is fine enough, there are still difficulties in estimating perimeter with local counting schemes.

Case 2: Improving resolution DOES NOT improve perimeter estimate.

Now consider the problem of determining the perimeter of a polygonal shape represented on a plane tiled with squares, as in Figure 1-5A. Computing the city block distance, we see that the estimated distance from point X to point Y in Figure 1-5A is four times the side of the large square pixels which tessellate the plane, comprising one east-west block and three north-south blocks between the two points. In fact, for two points which span an integral number of pixels, we can write the estimated

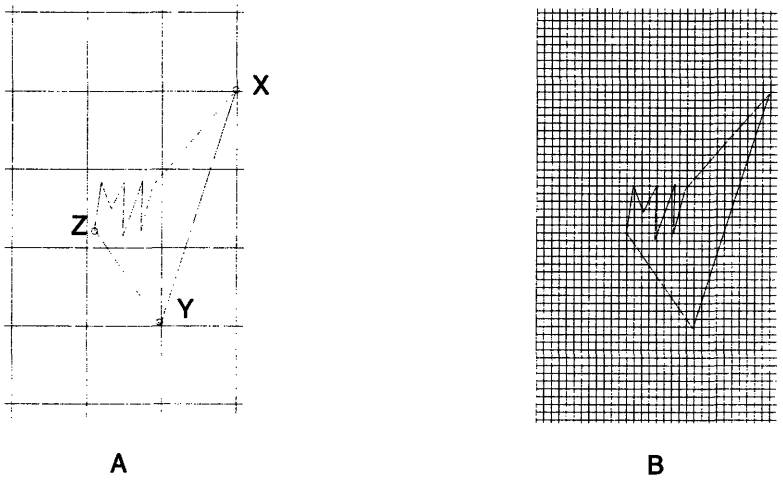

Figure 1-5: A polygon represented on two square grids of different resolution. Notice that the city block distance is the same on both grids for the line segment between points X and Y, but different for the sides between points X and Z. This results from the inability of the coarse grid in A to represent the fine details of the polygon.

length of a line segment between them on a square grid as:

$$L_S(R,\theta) = R\cos\theta + R\sin\theta \tag{1.3}$$

where θ is the angle the line segment makes with the x-axis, R is the true length of the line segment, and the subscript S denotes that the computation occurred on a square grid. If we prescribe the line to have unit length then the formula reduces to

$$L_S(\theta) = \cos\theta + \sin\theta. \tag{1.4}$$

It is apparent that the city block distance computation will be the same whether we use the grid in Figure 1-5A or Figure 1-5B, since *the formula does not depend on the pixel size.* Hence, for segments which span an integer number of pixels, the *estimated length is independent of grid size!* The same is true for a hexagonal tessellation, and also holds for surface area estimates in 3D tessellations.

It is a common mistake to assume that as the grid grows finer and finer, perimeter estimates will converge to the true perimeter. For example, Koplowitz et al. [10] state:

If the digitization resolution is high, i.e., the pixel size is small compared to the details of objects of interest, the digitized representation of their shapes is accurate and so will be the measurements of various shape parameters.

As we have seen, this is not true for local counting algorithms, and so the problem of finding the grid which gives the least error becomes more interesting.[2] In particular, note the inequality in the following expression:

$$\lim_{n\to\infty} L'_n(f) \neq L(f), \tag{1.5}$$

where $L'_n(f)$ is the approximate perimeter or length based on a local counting algorithm, and $L(f)$ is the length or perimeter of the figure or line segment.

This inequality suggests that we must consider other methods for obtaining accurate perimeter estimates for discretized figures. One approach is to look for tessellations which minimize the errors in estimated perimeter.

There is an analogous situation in three dimensions. Functions computable with local counting schemes in two dimensions (area, perimeter, and 2D Euler number) have analogous functions in three dimensions: volume, surface area, and 3D Euler number. Of these, only surface area has the property that it cannot be computed to arbitrary accuracy using a regular grid. That is, we cannot compute surface area to arbitrary accuracy by merely sampling a volume densely if we restrict ourselves to regular sampling and local counting algorithms.

[2]There are many ways to estimate the boundary of a figure from its tiled counterpart. Koplowitz et al. [10] give a review of these and present their own method. Some perimeter estimators produce much smaller errors, but they require each processor to have knowledge of a neighborhood of points. Other algorithms [11] use random or irregular tessellations whose perimeter error goes to zero as the number of pixels goes to infinity. However, here we restrict our analysis to local counting algorithms whose neighborhood is of size one and tessellations which produce uniform sampling of the plane and of space.

1.3 Organization of the Thesis

The accuracy and stability of local counting algorithms for perimeter estimation are affected by the size, shape, and position of the pixels one uses to tessellate the plane which contains the image. By choosing the tessellation carefully, we may be able to reduce estimated perimeter area for planar figures or estimated surface area for binary volumes. Square and rectangular pixels dominate modern image processing, but these standard pixel shapes are not necessarily optimal for all computations. In particular, hexagonal tessellations have many advantages [2] among which is a geometry which allows better perimeter estimates.

The focus here shall be on comparing tessellations in their optimality for the computation of boundary size. In two dimensions, this translates to perimeter estimation. There are a variety of meaningful functions on the boundary of a discretized planar figure which are related to the object's perimeter. In Chapter 2, each of these functions will be examined under square and hexagonal tilings.

After establishing the basic methods in two dimensions, we attack the same computations in three dimensions, specifically examining the estimation of surface area-dependent functions on arbitrary, piecewise smooth, binary 3-D volumes. This is the focus of Chapter 3. The hope is to find voxel shapes which allow us to estimated surface area of binary volumes with less error. Such volumes arise as outputs from 3D scanning devices like magnetic resonance imaging (MRI) and computed tomography (CT) scanners. For example, a simple thresholding operation on a set of CT images will give us a binary volume in which each white pixel represents bone and each black pixel represents some other, more X-ray-transparent tissue or substance. We analyze the accuracy of surface area estimates for objects in 3D binary volumes. We compare the results obtained from using a cubic tessellation of space to those using two alternative voxel shapes, the first employing the truncated octahedron and the second the rhombic dodecahedron.

In Chapter 4, we consider some implications and possible applications of the derived results.

Chapter 2

Two Dimensional Tilings

The main goal of this thesis is to present results regarding surface area computation on 3D grids. However, as is often the case in 3D geometry, this problem can be better understood by first carefully considering the results from the two dimensional analogs. Here we review some of the issues involved in computing perimeters of figures on square and hexagonal grids. These results will then be generalized to three dimensions, specifically considering cubic, truncated octahedral, and rhombic dodecahedral tessellations of space.

2.1 Choice of Tilings

There are an infinite variety of tilings to choose from when analyzing the perimeter estimation problem. Appendix A discusses some of the basic classes of tessellations and their associated grids. While the common Cartesian square grid and the hexagonal grid have many properties which make them convenient to use for tiling, we could find no proof in the literature that these were optimal for the perimeter estimation problem among tessellations which use a single tile shape. Nevertheless, a full treatment of 2-D tessellations is beyond the scope of this paper, and we choose to focus our efforts on the regular square and hexagonal tilings.

2.2 The Cartesian Square Tiling

We first consider square tessellations as represented in Figure A-1B. Again, let $L_S(\theta)$ be the estimated length of a unit length line segment computed using a local counting scheme on a square grid. If we assume (as discussed previously) that all orientations of line segments are equally likely with respect to the angle they make with the x-axis, then to compute the mean value for L_S over the range of all possible angles for the line, we integrate the equation for the estimated length of a unit segment (Equation 1.4) over the interval $[0, \pi/2]$ and divide by the interval of integration (see [9]):

$$\frac{\int_0^{\frac{\pi}{2}} L_S(\theta)d\theta}{\int_0^{\frac{\pi}{2}} 1d\theta} = \frac{\int_0^{\frac{\pi}{2}} (\cos\theta + \sin\theta)\, d\theta}{\frac{\pi}{2}} = \frac{(\sin\theta - \cos\theta) \mid_0^{\frac{\pi}{2}}}{\frac{\pi}{2}} = \frac{4}{\pi}. \tag{2.1}$$

We call this value the *mean length estimate* (for lines) or *mean perimeter estimate* (for figures) on a square grid. Alternatively, we can view this mean as a statistic of a random line-segment process, as is common in stochastic geometry (See, for example [22]). That is, if the line segments which approximate a planar figure have random and evenly distributed orientation θ and we want to compute the *expectation* of the length of those line segments as computed on a square grid, we have:

$$E\left[L_S\left(\theta\right)\right] = \int_0^{\frac{\pi}{2}} L_S\left(\theta\right) p\left(\theta\right) d\theta = \int_0^{\frac{\pi}{2}} L_S\left(\theta\right) \frac{1}{\frac{\pi}{2}} d\theta = \frac{4}{\pi}, \tag{2.2}$$

where the expectation is computed over the sample space of line segments.

On average, we overestimate the length of a line by a factor of $4/\pi \approx 1.273$ by using the city block estimate of length. We define the *length error*, which is just the difference between the true length of the line segment (which is defined to be 1) and the estimated length to be

$$e_{L_S}\left(\theta\right) = \left|L_S\left(\theta\right) - 1\right|. \tag{2.3}$$

Then the *expected length error*, or simply the *length bias*, is

$$E\left[e_{L_S}(\theta)\right] = E\left[|L_S(\theta) - 1|\right] = E\left[L_S(\theta)\right] - 1 = \frac{4}{\pi} - 1 \approx 0.273. \tag{2.4}$$

By symmetry, we can see that the length bias will be the same for lines whose defining orientation angle lies in the other three quadrants, so the same result is obtained whether we integrate over the full range of angles or merely in the first quadrant. Notice also that we could have limited the integration to the range $\theta \in [0, \pi/4]$ since the integrated functions are symmetric about the line $\theta = \pi/4$. In fact, any of the regions shown in Figure 2-1A serve as a basis for the interval of integration for Equation 2.2, as long as we add absolute value brackets around the sine and cosine functions.[1] This type of symmetry will be exploited in determining the surface area bias for truncated octahedron and rhombic dodecahedron tilings of space.

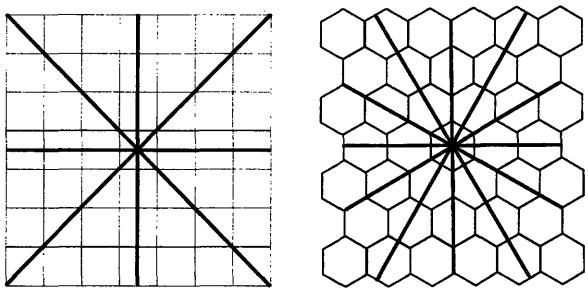

Figure 2-1: Bias symmetry regions for square and hexagonal tessellations. The recognition of such regions simplifies bias computations in more complicated tessellations. Notice that the hexagonal grid has twelve symmetry regions while the square grid has only eight.

2.3 Hexagonal Tilings

Next consider the errors obtained when the plane is tiled with hexagons, as in Figure 2-2. We start by noticing that for lines of unit length which lie at an angle $\theta \in [0, \pi/6]$,

[1]This 8-way symmetry of the circle with respect to the Cartesian axes is exploited in other domains, such as in the fast Bresenham circle algorithm of computer graphics [4].

the following formula for estimated length holds:

$$L_H(\theta) = \frac{4}{3}\cos\theta. \tag{2.5}$$

The somewhat surprising conclusion is that only the run, and not the rise, of such a line is relevant to the computation of its estimated length! To see this, note that each line which lies in the interval $\theta \in [0, \pi/6]$ (L1 and L2 in Figure 2-2) can be estimated by the hexagonal grid pieces in Figure 2-3. Each of these pieces is 4/3 as long as the distance between pixel centers along the x-axis, resulting in Equation 2.5. These hexagonal grid pieces are analogous to the east-west and north-south segments used for computing city block distance on a square grid.

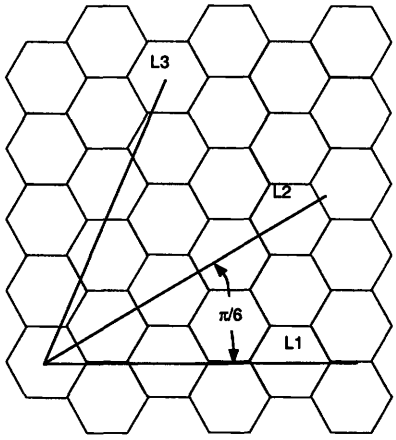

Figure 2-2: Lines on a hexagonal grid. For lines which lie at an angle between $\theta \in [0, \pi/6]$ radians from the x-axis, the estimated length is a constant times the length of the line projected onto the x-axis.

Unfortunately, the relationship of the hexagons to the coordinate axes becomes fundamentally different when the angle of the line is greater than $\pi/6$. The line L3 in Figure 2-2 cannot be represented as a sum of the hexagonal grid pieces of Figure 2-3. This leads to a more complex function for estimated length in the region

Figure 2-3: These two sections of the hexagonal grid, laid end to end, can be used to approximate any line segment which forms an angle $\theta \in [0, \pi/6]$ with the x-axis.

$\theta \in [\pi/6, \pi/2]$:[2]

$$L_H(\theta) = \frac{2}{3}\cos\theta + \frac{2}{\sqrt{3}}\sin\theta. \tag{2.6}$$

For our mean estimated length for the entire interval $\theta \in [0, \pi/2]$, we then have a combination of Equations 2.5 and 2.6:

$$\frac{\int_0^{\frac{\pi}{6}} \frac{4}{3}\cos\theta d\theta + \int_{\frac{\pi}{6}}^{\frac{\pi}{2}} \left(\frac{2}{3}\cos\theta + \frac{2}{\sqrt{3}}\sin\theta\right) d\theta}{\int_0^{\frac{\pi}{6}} 1 d\theta + \int_{\frac{\pi}{6}}^{\frac{\pi}{2}} 1 d\theta} = \frac{\frac{2}{3} + \frac{4}{3}}{\frac{\pi}{2}} = \frac{4}{\pi}. \tag{2.7}$$

Remarkably, this is the same mean length estimate as for the square. Again, in probability notation, we have:

$$E[L_H(\theta)] = \int_0^{\frac{\pi}{2}} L_H(\theta)\, p(\theta)\, d\theta = \int_0^{\frac{\pi}{2}} L_H(\theta)\, \frac{1}{\frac{\pi}{2}} d\theta = \frac{4}{\pi}. \tag{2.8}$$

Our real quarry, however, is the *hexagonal length bias* which is easily derived from the mean estimated length:

$$E[e_{L_H}(\theta)] = E[|L_H(\theta) - 1|] = E[L_H(\theta)] - 1 = \frac{4}{\pi} - 1 \approx 0.273. \tag{2.9}$$

While the function for the estimated length of lines with $\theta \in [\pi/6, \pi/2]$ is substantially more difficult to derive than for the interval $\theta \in [0, \pi/6]$, we note that they result in the same mean estimated length over the separate intervals by examining the numerical values of the integrals in the numerator of 2.7 (they both have mean $4/\pi$). Looking at the geometry again (Figure 2-1B), we can see that there is symmetry in the hexagon we could have taken advantage of, similar to that of the square. The general mean estimated length (for all angles) can be computed by computing only the mean estimated length for $\theta \in [0, \pi/6]$. All of the symmetry regions which have the same mean estimated length are shown in Figure 2-1B. We emphasize this

[2]The derivation of this formula is messy and not of particular interest, so we do not present it here. In fact, we present it mainly to emphasize that we want to avoid computing these types of formulas. Symmetry will be our main tool in avoiding these types of analyses.

point here because using this symmetry will be critical in simplifying surface area bias computations for truncated octahedral and rhombic dodecahedral tilings. Finding equations for estimated area over the set of all possible planar segments in three dimensions is substantially more complex than the comparable problem for hexagons in two dimensions.

2.4 Length Bias vs. Centered Length Bias

At first glance, one might conclude that the hexagonal tiling is no better than the square tiling, since they have the same length biases. However, we can make an improvement to our estimated length function on each grid by noticing that the estimated length is almost always[3] an overestimate of the true length. We define a new function of the line segment-valued random variable called the *centered estimated length* which we define for a square grid as:

$$L_S^{cent.}(\theta) = \frac{\sin\theta + \cos\theta}{K_S}, \tag{2.10}$$

where K_S is a correction factor for the overestimate.

The *centered length error* is then

$$e_{L_S^{cent.}}(\theta) = \left| \frac{\sin\theta + \cos\theta}{K_S} - 1 \right|, \tag{2.11}$$

such that, for appropriate values of K_S (a little bit larger than 1), $e_{L_S^{cent.}}$ should have a lower mean value than the previously defined error measure. That is, by assuming that the true length of a line segment is a little bit less than the value actually obtained from the local counting algorithm, we are likely to be closer to the true line

[3]For a square grid, the length of segments which align with the coordinate axes will match exactly the estimated length.

segment length. More formally, the *expectation of the centered length error* is:

$$E\left[e_{L_S^{cent.}}(\theta)\right] = \int_0^{\frac{\pi}{2}} \left| \frac{\sin\theta + \cos\theta}{K_S} - 1 \right| \frac{1}{\frac{\pi}{2}} d\theta, \tag{2.12}$$

which we call the *centered bias* for the square tiling. We define K_S to be the value which minimizes this expectation. K_S is difficult to obtain analytically due to the absolute value within the integral. However, evaluating numerically using a commercial math package [25], we obtain $K_S \approx 1.323$, and $E\left[e_{L_S^{cent.}}(\theta)\right] \approx 0.0798$, implying that even after centering, we can expect an error of approximately 8 percent in the length of lines or the perimeter of a figure on a square grid. Summarizing, the integral above represents the mean magnitude of the difference between the true length of the line, which we have defined to be 1, and the centered estimated length.

On a hexagonal grid, the centered estimated length becomes:

$$L_H^{cent.}(\theta) = \frac{\frac{4}{3}\cos\theta}{K_H}, \tag{2.13}$$

and the centered length error on the hexagonal grid is:

$$e_{L_H^{cent.}}(\theta) = \left| \frac{\frac{4}{3}\cos\theta}{K_H} - 1 \right|. \tag{2.14}$$

The expected value of this error, the centered bias for the hexagonal grid, is:

$$E\left[e_{L_H^{cent.}}(\theta)\right] = \int_0^{\frac{\pi}{6}} \left| \frac{\frac{4}{3}\cos\theta}{K_H} - 1 \right| \frac{1}{\frac{\pi}{6}} d\theta. \tag{2.15}$$

Here, through numerical methods again, we obtain $K_H \approx 1.291$, and $E\left(L_H^{cent.}(\theta)\right) \approx 0.0348$. Hence, tiling with hexagons does improve the mean accuracy of length estimates by almost five percent over the square tiling. This corresponds nicely with the intuition that representations with "more circular" pixels (i.e., the hexagonal ones) should demonstrate less sensitivity to line orientation.

2.5 Error Extrema and the Squared Centered Bias

Before moving on to 3-D tessellations, we examine a few more statistics for hexagonal and square tilings, the error extrema and the squared centered bias.

2.5.1 Error Extrema

In many engineering applications, one is concerned with minimizing the worst possible error in measurement. For example, in buying expensive paint to cover an irregularly shaped object, one may want to guarantee that one has enough paint before the project begins. Hence the measurement of the object which produces the smallest maximum possible surface area for a given measured area is desirable. This idea also applies to perimeter estimates.

Suppose we compute the city block distance of a line segment and obtain a value of 1. We do not know the actual length of the line segment which generated this measurement. It could be as short as $1/\sqrt{2} \approx 0.707$ and as long as 1. Hence, if we want to prepare for the maximum possible boundary length for a given measurement we need to commit to about 41% more than might actually be needed. For the hexagonal tiling, if a line segment measured 1 according to a local counting algorithm, the actual length would be at least 3/4 and at most $\sqrt{3}/2$. In this case, the maximum is only about 15% greater than the minimum, so the potential for waste is much smaller. Other quantities, such as the expected waste, favor the hexagonal grid. We include in Table 2.1 four statistics related to error extrema for square and hexagonal grids: the minimum and maximum length estimate errors and the minimum and maximum centered length estimate errors. These four quantities give a basic intuition about some of the behaviors of these tilings.

2.5.2 Squared centered error

An alternative to the centered error discussed previously involves weighting large errors more heavily than small errors. To do this we can merely square the residue

used in previous expressions. This gives us

$$e_{L_S^{sq.}}(\theta) = \left(\frac{\sin\theta + \cos\theta}{K_S} - 1\right)^2, \tag{2.16}$$

for the square grid, with an expectation of

$$E\left[e_{L_S^{sq.}}(\theta)\right] = \int_0^{\frac{\pi}{2}} \left(\frac{\sin\theta + \cos\theta}{K_S} - 1\right)^2 \frac{1}{\frac{\pi}{2}} d\theta, \tag{2.17}$$

which we call the *squared centered error.*

The value which minimizes the above equation (K_S) represents the "best" adjustment of our guess at the true length of the line given that we want to weigh larger errors more heavily. By differentiating Equation 2.17 with respect to K_S and setting it equal to 0 we find that the value of K_S which minimizes the expression is $\pi/4 + 1/2 \approx 1.285$, which makes sense, since we expected a value a little greater than 1. And this corresponds to an expected value of exactly $\frac{\pi^2+2\pi-16}{\pi(\pi+2)}$, which is approximately 0.00946.

For the hexagonal grid, we have an error measure of:

$$e_{L_H^{sq.}}(\theta) = \left(\frac{\frac{4}{3}\cos\theta}{K_H} - 1\right)^2. \tag{2.18}$$

with an expectation of:

$$E\left[e_{L_H^{sq.}}(\theta)\right] = \int_0^{\frac{\pi}{6}} \left(\frac{\frac{4}{3}\cos\theta}{K_H} - 1\right)^2 \frac{1}{\frac{\pi}{6}} d\theta. \tag{2.19}$$

Again, differentiating and equating to 0, we can obtain a value for K_H which defines our best guess for true length: $K_H = \frac{\sqrt{3}}{3} + \frac{2\pi}{9} \approx 1.275$. And again, this is a value slightly greater than 1. This generates an expected value of exactly $\frac{2\pi^2+3\sqrt{3}\pi-36}{\pi\left(3\sqrt{3}+2\pi\right)}$, which is approximately 0.00176. Thus, for this and higher order weightings of error magnitude, the hexagonal tiling becomes more advantageous.

	Square		Hexagon	
Statistic	**Closed Form**	**Approx.**	**Closed Form**	**Approx.**
Mean Length Estimate	$\frac{4}{\pi}$	1.273	$\frac{4}{\pi}$	1.273
Maximum Error	$\sqrt{2}-1$	0.414	$\frac{1}{3}$	0.333
Minimum Error	0	0.0	$\frac{2\sqrt{3}}{3}-1$	0.155
Length Bias	$\frac{4}{\pi}-1$	0.273	$\frac{4}{\pi}-1$	0.273
Optimal Centering Constant	–	1.323	–	1.291
Maximum Centered Error	–	0.244	–	0.134
Minimum Centered Error	0	0.0	0	0.0
Centered Bias	–	0.0798	–	0.0348
Squared Centered Bias	$\frac{\pi^2+2\pi-16}{\pi(\pi+2)}$	0.00946	$\frac{2\pi^2+3\sqrt{3}\pi-36}{\pi\left(3\sqrt{3}+2\pi\right)}$	0.00176

Table 2.1: Some estimated length statistics of a random unit-length line segment process under square and hexagonal tessellations. Notice that while the square and hexagonal grids have equal length bias, the hexagonal grid has a lower centered length bias as well as a smaller range of possible values for length estimates of a unit-length line segment.

2.6 Summary of results for 2-D

Table 2.1 summarizes the results for the perimeter statistics computed in this chapter. While one could compute many other statistics, these capture many of the important practical measures.

Chapter 3

Three Dimensional Tilings

We now turn to the problem of estimating the surface area of a volume on a discrete grid in three dimensions using a local counting scheme. The basic procedure is for each voxel to report the amount of its own surface area which is part of the surface area of the global object. Measurements of surface area will be biased again due to the discretization of the volume. Just as we assumed in Chapter 2 that planar figures could be well approximated by a finite number of fixed length line segments, we assume in 3-D that the volumes can be well approximated by *planar patches* or *planar segments* of arbitrary orientation and shape but of fixed area. Volumes for which this is not true are not addressed by the analysis in this paper. For example, fractal surfaces and other highly convoluted surfaces are not subject to the following analyses.

3.1 Cubic Tilings

Assume the true area of a planar segment is unity. Let θ and ϕ define the normal to the planar segment, as one would define a point on the unit sphere by two angles. Such a patch and the associated angles can be seen in Figure 3-1. The estimated area of this planar segment using a local counting algorithm on a cubic grid is then:

$$A_C(\theta, \phi) = \sin\phi + \cos\phi\cos\theta + \cos\phi\sin\theta, \tag{3.1}$$

assuming (as in the 2-D case with pixels) that the voxel size is small relative to the

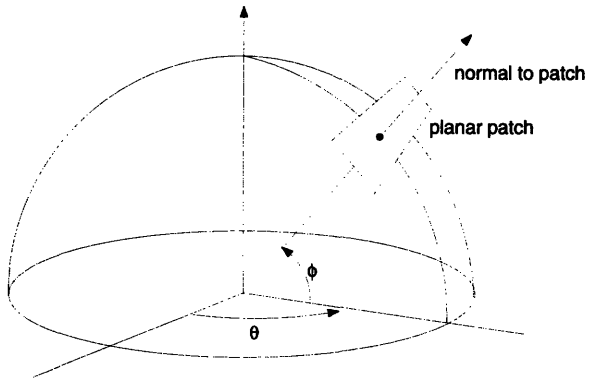

Figure 3-1: A planar patch and its associated angles.

size of the planar segment. The three terms on the right hand side of Equation 3.1 are the projections of the planar segment onto each of the primary Cartesian planes (x-y, y-z, x-z) respectively. This projection process is analogous to finding the city block length estimate in two dimensions.

3.1.1 Mean Estimated Area

Integrating Equation 3.1 over the angles θ and ϕ in the interval $[0, \pi/2]$ and dividing the result by the solid angle (in units of steradians) over which we have integrated gives us the *mean area estimate* obtained with a cubic grid. We need to multiply the area expression by the Jacobian term, $\cos\phi$, which handles the foreshortening of area as we approach the "north pole" of the unit sphere.[1] We have

$$\frac{\int_0^{\frac{\pi}{2}}\int_0^{\frac{\pi}{2}} A_C(\theta,\phi)\cos\phi\, d\phi\, d\theta}{\int_0^{\frac{\pi}{2}}\int_0^{\frac{\pi}{2}} \cos\phi\, d\phi\, d\theta} = \frac{\int_0^{\frac{\pi}{2}} \frac{1}{2} + \frac{\pi}{4}(\sin\theta + \cos\theta)\, d\theta}{\int_0^{\frac{\pi}{2}} 1 d\theta} = \frac{\frac{\pi}{4}+\frac{\pi}{2}}{\frac{\pi}{2}} = \frac{3}{2}. \tag{3.2}$$

We again offer an alternative interpretation of this mean surface area estimate as the expectation of a function of a random process which generates a uniform

[1] In the terminology of stochastic geometry, we say that the *differential form* $\cos\phi\, d\phi\, d\theta$ is the *density* of planar segments tangent to the unit sphere which is invariant under rigid motions of the coordinate axes. This is hence called the *uniform density* of this set of planar segments. See [23, page 118].

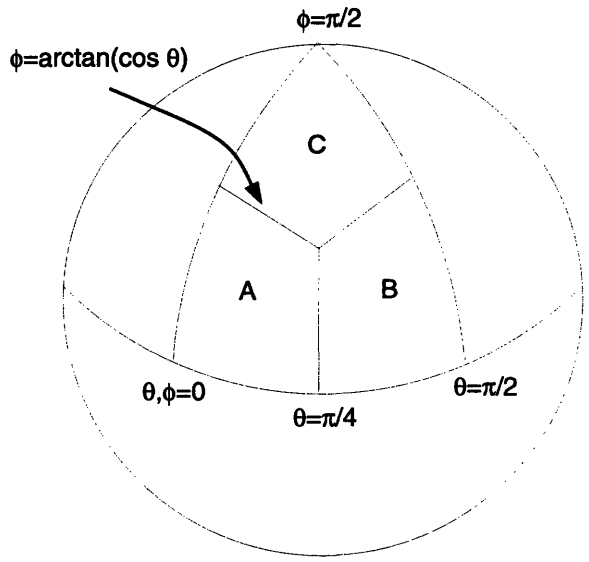

Figure 3-2: Integrating the estimated area expression in Equation 3.1 over the spherical triangle shown $\theta \in [0, \pi/2]\,; \phi \in [0, \pi/2]$ yields the area bias for planar segments on a cubic grid. We obtain the same result if we restrict the solid angle of integration to Area A, B, or C (area A is used in the text).

distribution of planar segments whose normals are distributed equally around the unit sphere. This interpretation yields the stochastic geometry view:

$$E\left[A_C\left(\theta, \phi\right)\right] = \frac{3}{2} \tag{3.3}$$

which is simply another framework for interpreting the results in this paper.

In the case of calculating the mean length estimate on a square grid in two dimensions, we noted that we could restrict our interval of integration to $\theta \in [0, \pi/4]$, due to the symmetry of a square grid. There is an analogous, albeit more complicated symmetry in 3-D on a cubic grid. Picture a sphere whose center is at the origin and whose equator lies in the x-y plane, as in Figure 3-2. The family of planar segments whose normals fall within the solid angle of Area A (or B or C for that matter) of Figure 3-2 have the same estimated areas and hence the same mean estimated area as the total family of planar segments whose normals lie in a single Cartesian octant. That is, just as the range $\theta \in [0, \pi/4]$ represents all of the unit length line segments needed to calculate the mean estimated length on a square grid, the part of the unit sphere defined by $\theta \in [0, \pi/4]\,; \phi \in [0, \arctan\left(\cos\theta\right)]$ represents a family of unit area

planar segments sufficient to calculate the mean estimated area on a cubic grid. To understand this, note that the function we are evaluating (from Equation 3.1) is symmetric with respect to the three coordinate axes. That is, if we relabel the axes and their associated angles, the value of the function integrated across the entire region remains the same.[2] This concept can be tested by integrating the equation for area bias over 1/3 of the spherical triangle shown in Figure 3-2, i.e. the solid angle which is represented by Area A. We should end up with the same mean area estimate which was computed in Equation 3.4, namely, 3/2. We see that this is in fact the case:

$$\frac{\int_0^{\frac{\pi}{4}} \int_0^{\arctan(\cos\theta)} A_C(\theta,\phi)\cos\phi\, d\phi\, d\theta}{\int_0^{\frac{\pi}{4}} \int_0^{\arctan(\cos\theta)} \cos\phi\, d\phi\, d\theta} = \frac{\frac{\pi}{4}}{\frac{\pi}{6}} = \frac{3}{2}. \tag{3.4}$$

This symmetry provides us with a slew of identities which can be found in Appendix B. These identities are helpful in deriving closed form solutions to area bias estimates for more complicated tilings which we shall encounter later.

3.1.2 Area Bias, Centered Area Bias, and Other Statistics

Once we have established the area estimation function and calculated the mean area estimate for a tiling, the computations of other statistics for that tiling follow straight forwardly. While it is not always easy to obtain a closed form solution for these statistics, at least numerical approximations can be obtained.

Since we described in detail the various statistics chosen for the square and hexagonal tilings in the plane, we omit repeating our exposition of these statistics for the cubic tiling, and merely present formulas and solutions for the additional statistics below. These results are summarized in Table 3.1.

[2] Actually, the smallest possible regions of symmetry are half the size of those shown in Figure 3-2. One can subdivide each of the Regions A, B, and C into smaller regions by drawing a great circle across the sphere from the center of the lune to the corner of the lune. This gives a total of six regions of symmetry per spherical octant, for a total of 48 regions of symmetry on the sphere. The six part symmetry is particularly apparent in Figure 3-11E and Figure 3-11F.

Area Bias for Cubic Tiling

We define the *area error* to be

$$e_{A_C}(\theta,\phi) = |A_C(\theta,\phi) - 1|, \tag{3.5}$$

and the expectation of this quantity, or *area bias*, is then

$$E[e_{A_C}(\theta,\phi)] = E[|A_C(\theta,\phi) - 1|] = E[A_C(\theta,\phi)] - 1 = \frac{3}{2} - 1 = 0.5. \tag{3.6}$$

Figure 3-3A shows the area error for a cubic tiling as a function of θ and ϕ, the two angles which define the normal to a planar segment. The color at each point represents the error for the planar segment defined by that particular point. For the cubic tiling, as expected, the error is zero at the three corners of the plot, since this corresponds to the three principal Cartesian planes, which can be perfectly represented in a cubic tiling. However, as the angle of the plane becomes more oblique, the error increases quickly. The maximum error occurs in the middle of the plot and has an area error of $\sqrt{3} - 1 \approx 0.732$. Figure 3-3B shows the benefit of centering the error which is discussed in the following section.

Centered Bias for Cubic Tiling

To produce the *centered area bias*, we must first define the *centered estimated area* to be

$$A_C^{cent.}(\theta,\phi) = \frac{A_C(\theta,\phi)}{K_C}, \tag{3.7}$$

where K_C is the correction factor for the overestimate of area. Then, the *centered area error* is:

$$e_{A_C^{cent.}}(\theta,\phi) = \left|\frac{A_C(\theta,\phi)}{K_S} - 1\right|, \tag{3.8}$$

and the expectation of this quantity is just

$$E\left[e_{A_C^{cent.}}(\theta,\phi)\right] = \int_0^{\frac{\pi}{4}} \int_0^{\arctan(\cos\theta)} \left|\frac{A_C(\theta,\phi)}{K_C} - 1\right| \frac{1}{\frac{\pi}{6}} \cos\phi \, d\phi \, d\theta. \tag{3.9}$$

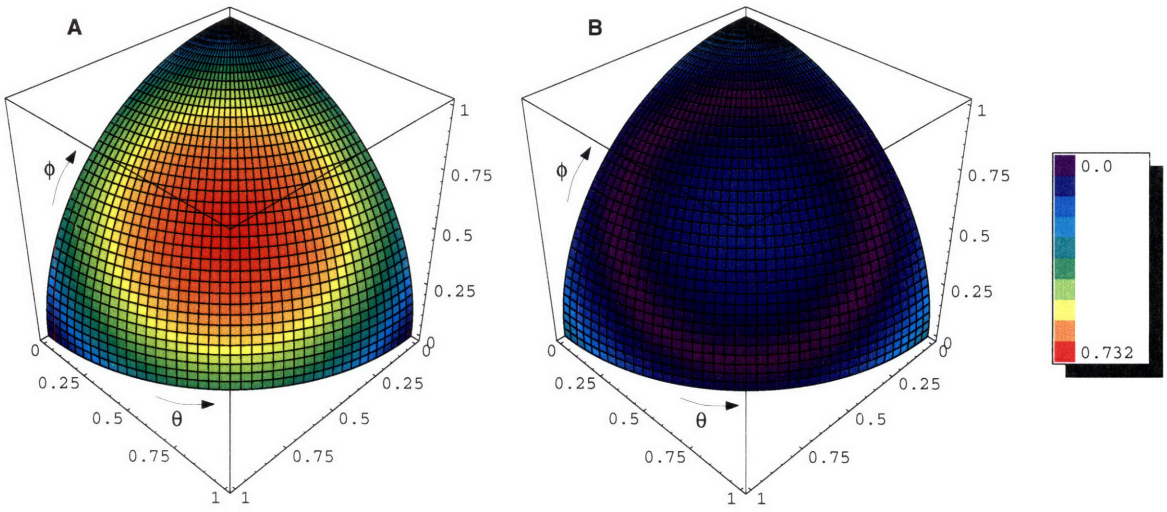

Figure 3-3: **A.** Area error as a function of the planar segment normals θ and ϕ for the cubic tiling. Notice that the error is zero at the corners which represent the principal Cartesian planes, but increases quickly as we move toward the plane defined by the equation $x+y+z=1$, which gives an area error of approximately 0.732. **B.** Centered area error as a function of θ and ϕ. The error is greatly reduced by the centering process. The maximum error is now only 0.348 and occurs in the corners of the plot. Notice the purple ring of zero error in the middle of the lune.

Minimizing over K_C using numerical methods, we obtain $K_C \approx 1.533$ corresponding to a *centered area bias* of approximately 0.0812. Figure 3-3B shows a plot of the centered area error as a function of the planar segment normals. Notice the greatly reduced error due to the correction factor.

Squared Centered Bias for Cubic Tiling

Following in the same vein, we compute the *squared centered error* for area, as

$$E\left[e_{A_C^{sq.}}(\theta,\phi)\right] = \int_0^{\frac{\pi}{4}} \int_0^{\arctan(\cos\theta)} \left(\frac{A_C(\theta,\phi)}{K_C} - 1\right)^2 \frac{1}{\frac{\pi}{6}} \cos\phi \, d\phi \, d\theta, \qquad (3.10)$$

The value of $K_C \approx 1.516$ minimizes the expression, which has a corresponding value of approximately 0.0102.

Error Maxima and Minima for Cubic Tiling

In two dimensions, computing the values of θ which maximized and minimized our estimated length functions was easy since these functions are monotonic over the relevant range of θ. In three dimensions, this same statement holds for the partial derivatives (with respect to ϕ and θ) of the cubic grid estimated area function, so again we have it easy:

$$\max_{\phi,\theta} A_C(\theta,\phi) = A_C\left(\frac{\pi}{4}, \arctan\left(\cos\frac{\pi}{4}\right)\right) = \sqrt{3}, \tag{3.11}$$

and

$$\min_{\phi,\theta} A_C(\theta,\phi) = A_C(0,0) = 1. \tag{3.12}$$

These values give us a maximum centered error of approximately 0.348, and the minimum centered error is of course 0.

3.1.3 Summary of Results for Cubic Grid

Let us pause for a moment to consider the meaning of some of these results. First, the expected error when we simply compute area of a smooth figure on a cubic grid using a local counting scheme is exactly 50 percent. While this is large, we can do substantially better by dividing the result of the local counting algorithm by 1.533 and using this as our guess of the true area. Our expected error is then only about 8 percent, a great improvement. However, as we shall see, we can do substantially better than this. Furthermore, our worst case error, even after centering, is still 34 percent, which is quite severe for some applications. This too, we would like to improve upon.

3.1.4 Other Choices of Grids

Suppose we choose something other than the standard Cartesian cubic grid for our tessellation. Can we reduce the area bias of planar segments represented with different voxels or a different arrangement of voxels? What are reasonable choices for voxel

shapes?

What More Can We Do with Cubes?

Note that even using cubes, we can achieve alternative tessellations with interesting properties by sliding planes of cubes and rows of cubes relative to other planes and rows (Again, this is suggested by Horn [9]). Using cubes we can generate grids which have neighborhood properties equivalent to the truncated octahedron tiling which we explore below. Although we do not investigate the issue here, we conjecture that the surface area bias of a cubic voxel grid arranged in the geometry of a truncated octahedron tiling has greater surface area bias than the corresponding truncated octahedron grid.

Perhaps a more interesting topic for future work would be an analysis of cubic grids with random planar and row-wise displacements. The two dimensional analog would be a brick wall whose successive layers were displaced randomly. We suspect that these configurations may actually be optimal for many problems, but an analysis of these configurations is beyond the scope of this paper.

Affine Transformations of Cubes

Now it is easy to see that any affine transformation of a tessellation is also a tessellation. (For more on tessellations, see Appendix A.) We can break these transformations down into translation, rotation, scaling, shearing, and reflection. Translation, rotation, and reflection of grids are not very interesting since they lead to identical area bias analyses. And we already know that the size of pixels and voxels do not affect boundary estimates when the tiles are "small" relative to the tessellated figure (Chapter 2), so scaling our cubic voxels will not yield an improvement in area bias.

Non-uniform scaling of the Cartesian cubic grid yields the interesting case in which the voxels are rectangular prisms, which is probably the most common situation in the data obtained from many sources, including most medical scanners, such as MRI and CT scanners. The somewhat surprising result here is that the area bias for rectangular prism voxels is equivalent to that of cubes. This is easily seen by realizing

that the estimated area function for rectangular prism voxels is the same as that for the cube (Equation 3.1). This seems quite counterintuitive (at least it did to me!). The resolution of this conundrum is that in practice, the largest cubic voxel volume which gives a surface area estimate within some tolerance ϵ will fail to achieve this tolerance for a non-cubic rectangular prism voxel. That is, the voxels must be smaller for rectangular prism voxels to achieve the same performance. However, if we start with the assumption that the voxels are "small enough" which has been our running assumption, then the two tessellations are equivalent.

Tessellations with parallelepipeds are not considered here, but again, we suspect that these will do no better than their correspondingly arranged cubic counterparts. That exhausts the possibilities for cubes and their affine transforms. There are many other groups of polyhedra which tile space however. Some of these can also tile space in more than one manner.

The Regular Polyhedra

There are exactly five regular polyhedra (also called the Platonic solids); they are defined as polyhedra in which each face is the same regular polygon[24]. These polyhedra have many properties which make them good candidates for analysis. Unfortunately, among these solids (tetrahedron, cube, octahedron, dodecahedron, and icosahedron), only the cube tiles space, so we have completed our analysis of tessellations for this class of polyhedra.

The Semi-Regular Polyhedra

Another interesting class of solids are the semi-regular polyhedra. There are various definitions in the literature, but Lyusternik [16, page 147] gives the definition as "a polyhedron all of whose faces are regular polygons (though all faces need not be of the same type) and all of whose polyhedral angles are equal." Properties of these solids and the regular polyhedra can be found in [5, 16, 24].

Of these, three tile space: the triangular prism, the hexagonal prism, and the truncated octahedron. We have chosen to analyze the truncated octahedron here

because of its symmetry properties. An analysis of the prisms seems warranted at some point, however. For now, we turn to the analysis of the truncated octahedron. The hope is that given its more "spherical" shape, it may have less of a centered area bias than the cube.

3.2 The Truncated Octahedron

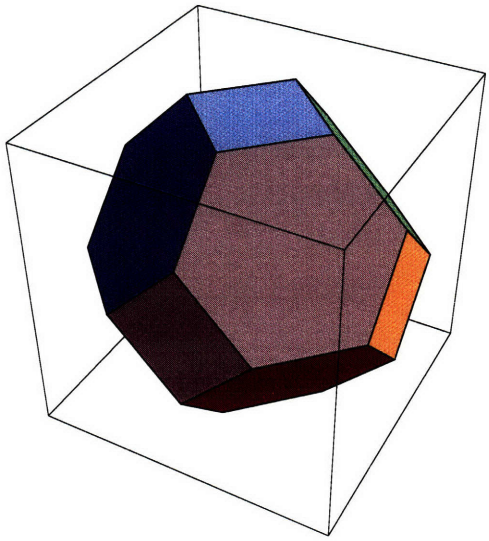

Figure 3-4: A truncated octahedron.

A truncated octahedron (TO) is shown in Figure 3-4. It has 14 sides, eight of which are squares and six of which are regular hexagons. Hence as mentioned before, it is a semi-regular polyhedron. It can be constructed by chopping off (*truncating*) the corners of a regular octahedron so that the edge length is reduced to 1/3 of the original.

We have already hinted that one may encounter some challenges in evaluating the surface area bias for a TO tiling of space. The primary difficulty encountered is very similar to the one already discussed for the hexagonal tiling of the plane, in which one encounters a fundamental change and increased complexity in the estimation of area for certain orientations of planar segments. In three dimensions the problem is exacerbated by the difficulty of drawing multiple layers of objects. A simple solution to this problem relies again on finding certain symmetries in the tiling which we can

exploit.

3.2.1 The Estimated Area Function for Truncated Octahedral Grids

Unlike the square, the cube, and the hexagon, it is not immediately obvious how to align the TO's with respect to the coordinate axes to simplify our analysis of estimated surface area. Figure 3-5 shows several possibilities, assuming the viewer is looking down along the z-axis, from a point P at $(0,0,1)$. The one shown on the far right is of particular interest, since it is symmetric with respect to the three coordinate axes. That is, in this orientation, the TO would look exactly the same if projected onto any of the three principal Cartesian planes. This feature greatly simplifies the computation of the estimated area of a planar segment tiled with TO's.

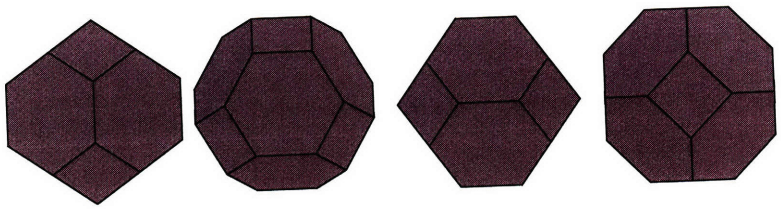

Figure 3-5: Four views of a truncated octahedron. The choice of orientation of this solid relative to the coordinate axes can significantly affect the complexity of the analysis of surface area bias. Because it is symmetric with respect to the three coordinate axes, the orientation shown in the rightmost drawing is used in this paper.

Another key property of this particular orientation of the TO is that for the discretization of a plane which forms an angle of less than $\pi/4$ with the x-y plane (exactly those planes whose normals lie in Region C of Figure 3-2), if we view the tiling from the z-axis, that is, from a point P at $(0,0,1)$, *we can see every voxel (but not necessarily every exposed facet of each voxel) which is part of the surface representation.* That is, the projection of the surface onto the x-y plane contains part of every voxel which is part of the surface representation. That is, there are no "hidden voxels" as there would be for the representation of planes at steeper angles, or with different orientations. This projection will always look something like the diagram in Figure 3-6. In particular, all of the exposed hexagonal facets will be

visible, and all of the square facets which are parallel to the x-y plane will be visible. This is critical in that it allows us to count the contribution to area made by these faces from a projection of the tessellated plane.

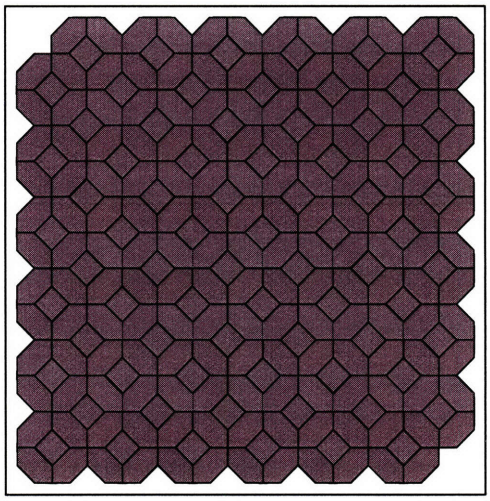

Figure 3-6: A part of a surface represented with truncated octahedra as described in the text. The view is from any of the coordinate axes.

To get a better feel for this phenomenon, first examine Figure 3-7. This represents the intersection of a TO tiling of a planar surface with the x-z plane. Notice that the angle $\theta < \pi/4$. The viewer from above will always be able to see each voxel which is part of the surface. In fact, the projection of this surface contains an image of every facet of each voxel which is part of the planar representation, except for those facets marked as "invisible". Additional insights may be gained by referring to the figures in Appendix D, which provides several examples of projections of a tessellated planar patch onto different planes.

If we were only interested in the surface facets which were viewable from this angle, we could compute their area with the formula

$$A_{T_{xy}}(\phi, \theta) = \left(\frac{1}{4} + \frac{3}{4}\sqrt{3}\right) \sin\phi \tag{3.13}$$

since 1/4 of the projected area is covered by square faces of TO's whose projected areas are equivalent to their original areas and 3/4 of the projected area is covered by hexagonal faces of TO's which have been foreshortened by a factor of $\sqrt{3}$. However,

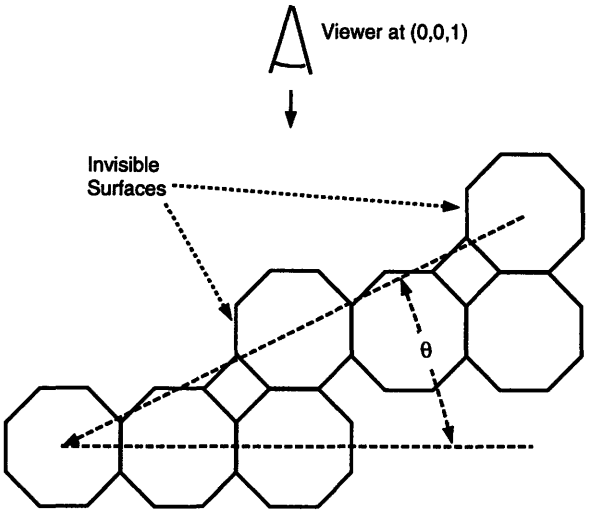

Figure 3-7: Intersection of TO tiling of a surface with the x-z plane. Notice that while all voxels which are part of the surface can be seen from above, not all facets of those voxels which contribute to the surface area can be seen.

this approach would miss the "invisible facets" shown in Figure 3-7. To compute their contribution to the surface area of the tessellated surface, we must view the surface from both the x- and y-axes as well. That is, we must project the surface onto both the y-z and the x-z planes and add area from these projections to the estimated area expression.

Adding together these three projections without modification will over-count the area, however, since the hexagonal facets which appear in the y-z and x-z projections also appear in the x-y projections. We do not want to count any facet more than once. Hence, we only count the portion of the projection which resulted from projecting the square facets for our second and third projections. This gives the formula:

$$A_T(\phi,\theta) = \left(\frac{1}{4} + \frac{3}{4}\sqrt{3}\right)\sin\phi + \frac{1}{4}\sin\theta\cos\phi + \frac{1}{4}\cos\phi\cos\theta, \quad \{\forall(\phi,\theta) \in C\}, \quad (3.14)$$

where C again represents Region C of Figure 3-2.

This formula only works because we are limiting our analysis to planes which form an angle of less than $\pi/4$ with the x-y plane. The best analogy here is again with the analysis of perimeter on a hexagonal grid in two dimensions. On a hexagonal grid, the simple formula for perimeter only holds for certain sets of line segments, those

which form an angle of less than $\pi/6$ with the x-axis. Again we refer the reader to Appendix D for additional figures which may elucidate the matter further.

Now that we have an expression for the estimated area at a particular pair of angles, θ and ϕ, we can integrate our expression for estimated area (A_T) over the appropriate solid angle interval, again using the proper Jacobian, to obtain the mean estimated area for a TO tiling:

$$\frac{\int\int_C A_T(\phi,\theta)\cos\phi\, d\phi\, d\theta}{\int\int_C \cos\phi\, d\phi\, d\theta} = \frac{\frac{\pi}{16} + \frac{3\sqrt{6}}{8} \times \arctan\frac{1}{\sqrt{2}}}{\frac{\pi}{6}} \approx 1.455. \tag{3.15}$$

(For a more detailed exposition of this result, refer to Appendix C.) As a check, we note that this result should be slightly greater than one, which it is. Interestingly, it is better (i.e. closer to 1) than the area bias for cubes.

3.2.2 Other Statistics on the TO Grid

As with the cubic tiling, it is interesting to examine a variety of statistics for the TO tiling. Since these are computed in a manner identical to that of the cubic tiling, they are simply summarized in Table 3.1. The most significant item to note in the table regarding the TO is that the centered area bias is significantly lower for the TO grid. This means we can estimate the area of an arbitrary binary volume significantly more accurately using a local counting algorithm on a TO grid than on a cubic grid. This is a very satisfying result. However, we may be able to do better yet!

3.3 The Rhombic Dodecahedron

Before concluding, we examine one last solid, the rhombic dodecahedron. It is pictured in Figure 3-8 . It has twelve sides, each of which is a rhombus, i.e. a quadrilateral with four equivalent sides. It is a dual of one of the semi-regular polyhedra, the cuboctahedron. It is also a special case of the *stellated cube*. It has many nice symmetry properties and is also a *zonohedron*, defined in [24]. This shape can be confusing to look at in part because several of its projections onto planes are identical to the

	Cube		Truncated Octahedron		Rhombic Dodec.	
Statistic	**Closed Form**	**Approx.**	**Closed Form**	**Approx.**	**Closed Form**	**Approx.**
Mean Area Estimate	$\frac{3}{2}$	1.500	$\frac{3}{8}+\frac{9\sqrt{6}}{4\pi}\arctan\frac{1}{\sqrt{2}}$	1.455	$\frac{3}{2}$	1.5
Maximum Error	$\sqrt{3}-1$	0.732	$\frac{\sqrt{30+6\sqrt{3}}}{4}-1$	0.589	$\frac{\sqrt{10}}{2}-1$	0.581
Minimum Error	0	0.0	$\frac{\sqrt{3}-1}{4}$	0.183	$\sqrt{2}-1$	0.414
Area Bias	$\frac{1}{2}$	0.500	$-\frac{5}{8}+\frac{9\sqrt{6}}{4\pi}\arctan\frac{1}{\sqrt{2}}$	0.455	$\frac{1}{2}$	0.5
Optimal Centering Constant	–	1.533	–	1.478	–	1.517
Maximum Centered Error	–	0.348	–	0.191	–	0.0701
Minimum Centered Error	0	0.0	0	0.0	0	0.0
Centered Bias	–	0.0812	–	0.0580	–	0.0318
Squared Centered Bias	–	0.0102	–	0.00462	–	0.00191

Table 3.1: Some statistics for random plane processes on tessellations of cubes, truncated octahedra, and rhombic dodecahedra.

projections of cubes. Hence from some angles, it looks exactly like a cube. This can be very confusing to the eye. Nevertheless, it does tile space, and we examine its properties here.

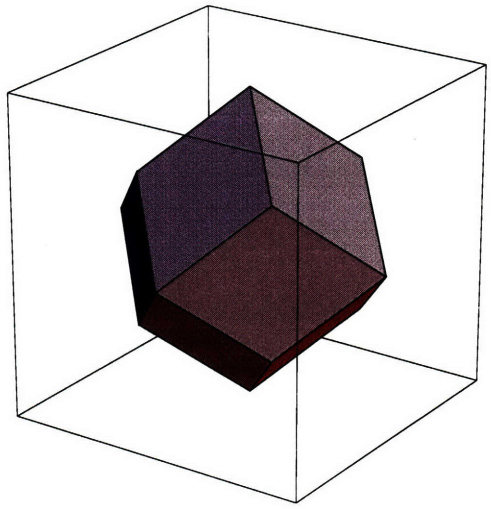

Figure 3-8: The rhombic dodecahedron.

3.3.1 The Estimated Area Function for Rhombic Dodecahedral Grids

As was the case for truncated octahedra, it turns out to be useful for the purposes of tessellation analysis to look for symmetries in the rhombic dodecahedron (RD) relative to the coordinate axes. As luck would have it, the RD also has a 3-D orientation such that the projection onto each of the three major Cartesian planes is equivalent. Figure 3-9 shows possible candidates for tiling orientations, and the orientation on the right has the desired property, i.e. it looks the same to a viewer from any of the coordinate axes.

Recall that for a TO tiling, all voxels which contributed to the surface area computation of a tessellated plane were at least partially visible from the z-axis. Also all of the facets which were not perpendicular to the line of sight (the "invisible facets") made a contribution to the projection of the tessellated plane onto the x-y plane. Given the above choice of orientation for RD voxels, we have the same situation for the RD grid. For a plane whose normal makes an angle of less than $\pi/4$ with the

z-axis and which is tessellated with RD's, each voxel which is part of the surface of that plane can be seen when the tessellated plane is viewed from infinity on the z-axis. Figure 3-10 shows the appearance of such a tessellation when viewed from the z-axis. As with the TO tiling, the part of the surface area which can be seen

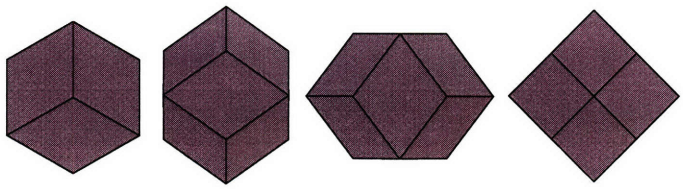

Figure 3-9: Projections of the rhombic dodecahedron.

from this limited perspective has a simple formula in terms of the projection of the plane. (Appendix D again offers additional renditions of a rhombic dodecahedron tiled planar segment projected onto several different planes.) Each rhombic facet is foreshortened by $\sqrt{2}$, yielding the following formula for planar segments of unit area whose normals are designated by (ϕ, θ):

$$A_{xy}(\phi, \theta) = \sqrt{2} \sin \phi. \tag{3.16}$$

However, as with the case of the truncated octahedron, Equation 3.16 does not capture all of the area which is part of the tessellated surface. That is, there are again certain "invisible" facets which are not captured by that projection. To measure the rest of the area, we must add in parts of other projections as well. It took a bit of experimentation to find the projections which allow one to count each face only once. It turns out that if we project the surface onto the planes whose equations are $x = z$ and $y = z$, we obtain exactly twice the area of the remaining uncounted area.

Hence, our new and complete formula for estimated area on the RD grid becomes

$$A_R(\phi, \theta) = \sqrt{2} \sin \phi + \frac{1}{2} \cos \phi \cos \left(\theta + \frac{\pi}{4} \right) + \frac{1}{2} \cos \phi \sin \left(\theta + \frac{\pi}{4} \right), \quad \{ \forall (\phi, \theta) \in C_L \}, \tag{3.17}$$

where the last two terms are 1/2 the projection onto the aforementioned planes. This expression can also be integrated (see Appendix C) to yield the results found in

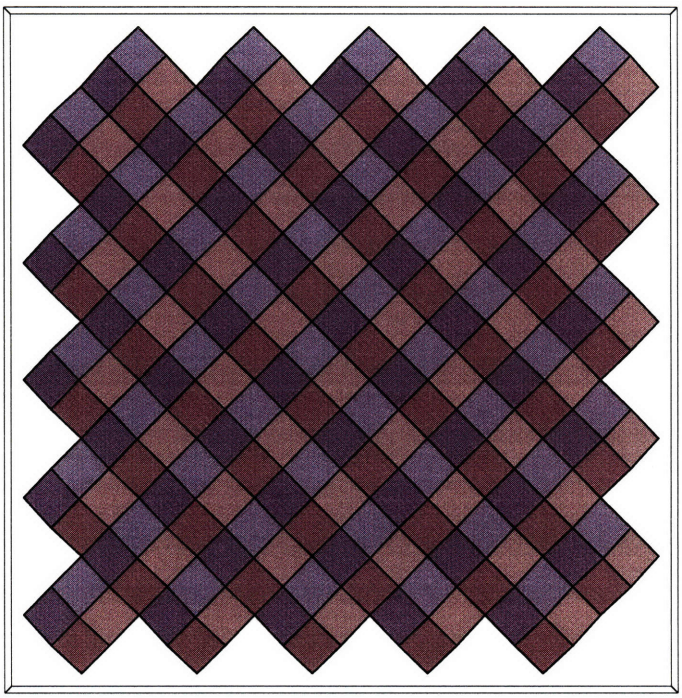

Figure 3-10: A surface tessellated with rhombic dodecahedra, as viewed from along the z-axis.

Table 3.1. Note that the equation is accurate only over a subset of the Region C from Figure 3-2. We call this Region C_L since it is the left half of Region C. Fortunately, it represents another (albeit smaller) of the "symmetry regions" discussed earlier. That is, integrating over it alone produces the correct mean area error. We refer the reader again to Figures 3-11E and F for an illustration of these smaller symmetry regions.

3.4 Summary of Results for 3-D

Examining Table 3.1, we see that while the truncated octahedron gives the best result for mean area estimate, the rhombic dodecahedron has a significantly smaller centered area bias and also a much smaller maximum centered error. This is a significant result if we are trying to minimize the error in surface area computation using local counting algorithms on a regular grid.

To understand these results visually, examine Figure 3-11. (NOTE: Figure 3-11 is best when viewed in color.) On the left of the figure are plotted the area errors of the cubic, truncated octahedral, and rhombic dodecahedral tilings as functions of

the planar segment normals. Notice that while the cube has the smallest errors of any of the plots (the error is zero at the corners of the lune), it also has the largest error (in the center). It also has a large variation in error. This implies that after centering the error, the other tessellations may do better. This is demonstrated on the right hand side of the figure, which shows the centered area error for each of the tessellations. In particular, notice that the rhombic dodecahedral centered error (F) has relatively low error throughout the entire plot. This gives some intuition to the result that the overall centered error bias is lower for the RD tiling.

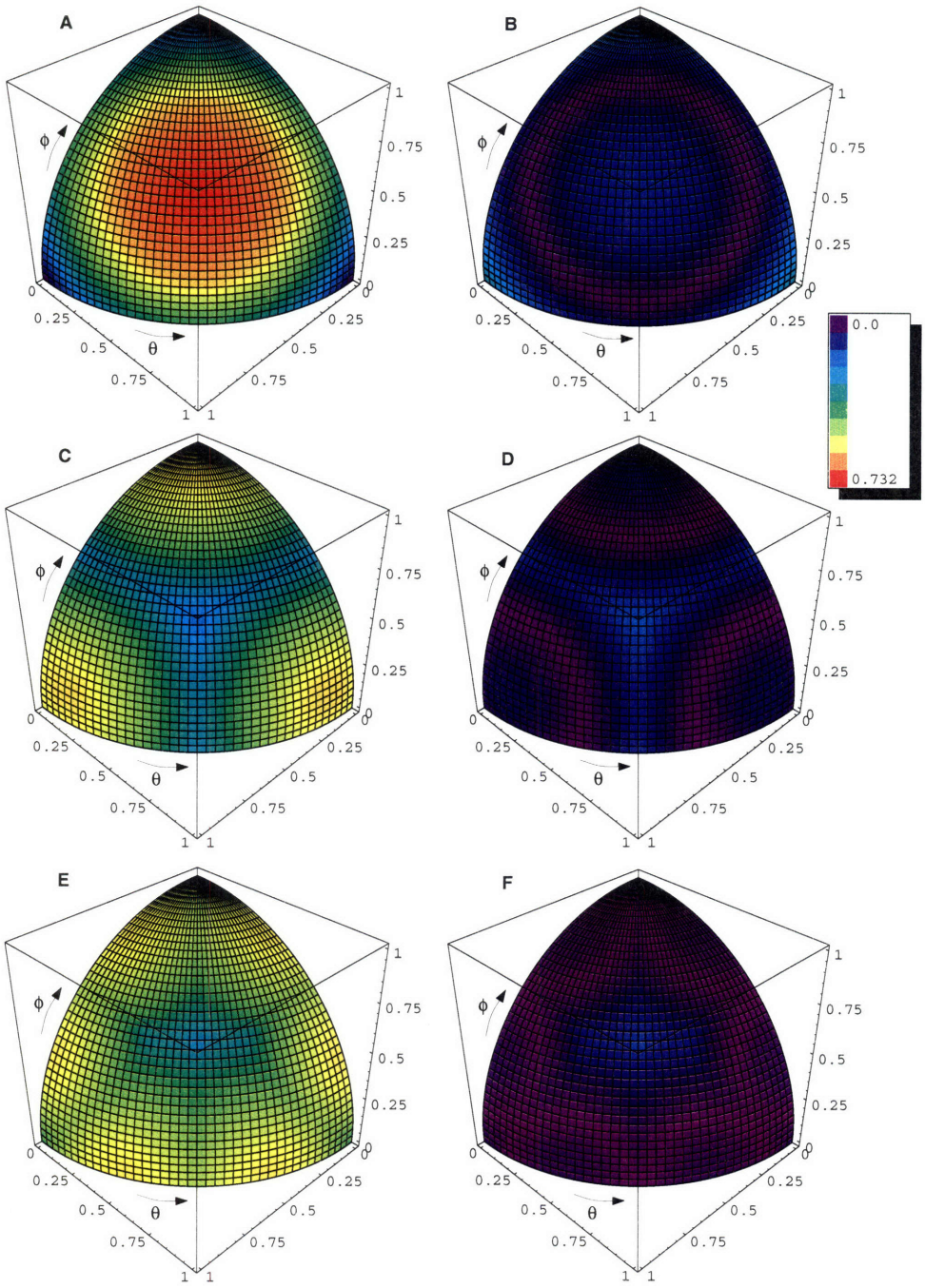

Figure 3-11: Estimated area error and centered estimated area error as a function of surface angle for different tessellations. **A.** Estimated surface area error for the cubic tiling. Notice that the errors are zero at the corners of the lune, which represent the errors for planes parallel to the three principal Cartesian planes. The mean error is large, however. **B.** The centered area error for cubes. The mean error is greatly reduced by centering the error. **C.** Surface area error for a TO tiling. Notice that the maximum error is reduced but the minimum error is increased. **D.** The centered surface area error for the TO tiling. **E.** Surface area error for the RD tiling. Notice the low variance in the error. **F.** Centered surface area error for the RD tiling. This tiling achieves the least centered area bias of the tilings we analyzed.

Chapter 4

Discussion and Applications

Given the results in Table 3.1, it is clear that the truncated octahedron and the rhombic dodecahedron tessellations produce more accurate surface area estimates for random planes and smooth binary 3-D volumes. While the main thrust of this paper is not applications, it is worth mentioning a few possibilities here.

The justification for this work is mostly of a "basic research" nature. Surface area is one of the most fundamental properties of solid volumes, and understanding it's computation under certain constraints may or may not prove fruitful. Some researchers have let their excitement about alternative tessellations in two dimensions get in the way of reason. That is, just because a tessellation has certain mathematical properties does not necessarily mean that it will be useful in a particular situation. In particular, some researchers lament the fact that virtually all modern imaging and display has been done on raster grids and displays. They hope that there is some way to "recover" the lost data from this sampling process and make use of it on a hexagonal grid. However, the original data is already gone. We cannot create more data by "resampling" on a hexagonal grid.

For example, Her and Yuan [8] espouse the advantages of a hexagonal grid relative to a square grid of the *same resolution.* But because, as they put it, "a real hexagonal grid device is very difficult to find", they proceed to discuss the advantages of creating a pseudo-hexagonal grid by combining pairs of pixels on a square grid. This process, however, can only destroy information. The resulting images will obviously have

poorer resolution, as the authors discuss. But the authors claim "in some cases, however, that better connectivity and symmetry properties in an image are no less important than the resolution itself." The only problem with this argument is that we could have obtained the exact same connectivity information directly from the original square grid without losing any information. The eagerness to apply the advantages of a new tessellation should not obscure the fact that it simply may not be worth it.

Hence, we must look for applications where the original continuous data is still available or for which hardware is not inherently rectangular, such as in raster displays. One of the most promising potential application areas which satisfies these requirements is in medical imaging.

4.1 Medical Applications

The advent of many volumetric medical imaging modalities (magnetic resonance imaging (MRI), computed tomography (CT), high resolution ultrasound imaging, etc.) have resulted in a large number of quantitative studies of 3D structures, for example see [18]. While many of these are based on volume measurements rather than surface area measurements, improving the accuracy of surface area estimates may make this measure more attractive. Petty et al. [20] studied surface area measurements of the *planum temporale* (a relatively smooth part of the brain) in schizophrenic patients as a correlate of disease. Such studies could presumably benefit from better surface area measurements, especially since analytical models of the surfaces being measured are unavailable.

Body surface area is commonly used in computing doses for various pharmaceuticals. This measure is commonly approximated using only a patient's weight and height. It would seem that a full body scan with a subsequent surface area analysis could yield a better estimate of surface area, if this expense were warranted. At a minimum, such techniques could be used to find more accurate correlates of true body surface area.

In medical applications, the original data (human tissue properties) are for all

practical purposes continuous. At some point these data must be discretized for analysis. If we cannot get access to the data before discretization, then alternative tessellations are of no use. Hence, for retrospective medical analysis, in which we only have the discretized medical images, we can think of no way to make an improvement in surface area estimates. However, MRI is acquired as frequency data and modifying the software to sample this data along a truncated octahedral grid or a rhombic dodecahedral grid may not be difficult.

4.1.1 The Practicality of Using TO and RD Voxels

At first glance, TO's and RD's appear much more complicated than cubic or rectangular prism voxels. However, many of the properties in which we are interested are not difficult to compute on these grids. For example, finding the voxel which contains a particular spatial point is just a matter of finding the nearest voxel center, since the TO and RD tessellations are both Dirichlet tessellations (see Appendix A). Also, keeping the voxels in a logically arranged order in memory may be of some concern. The realization that the centers of voxels in a TO tiling have positions equivalent to two interleaved rectangular prism grids and in an RD tiling have positions equivalent to four interleaved rectangular prism grids suggests a variety of relatively straightforward addressing schemes, such as keeping a pair of rectangular arrays for a TO tiling. We do not want to imply that there is no additional cost in using these tessellations, but only that many tasks are still manageable on these grids.

4.2 Industrial Applications

In the manufacturing world, there are a number of reasons why one may want to know the surface area of an irregularly shaped object. These include calculating flux of some physical quantity across or along a surface such as shear stress, heat or electromagnetic fields [1], computing wind resistance (as in the automotive industry), or merely needing to know how much paint or substrate one needs to cover an object. While in some engineering situations, a manufactured device is composed of objects

whose surface area is easily computable, this is not always the case [13, 14]. In these situations, application of the results presented here may be of some use.

4.3 Other Properties of the RD and TO Tilings

If the computation of surface area alone is not enough to justify a new representation for solids in a particular application, other properties of the RD and TO tilings may be enough to swing the balance.

4.3.1 Tessellation as Sampling

For example, we can view the process of voxelization in the signal processing context as a sampling. As implied by Mersereau and Dubois [19, 3], the TO and RD tilings are both more "efficient" spatial samplers than the cubic grid. That is, for a 3-D band-limited signal which is spherically symmetric in the frequency domain, we require fewer samples on a TO or RD grid to fully reconstruct the signal (that is, to meet the Nyquist sampling criterion for all spatial frequencies) than we do on a cubic grid. The number of samples needed is proportional to the volume of the minimum grid shape which can bound the unit sphere. For example, this is equal to 8.0 for a cubic tiling but only $4\sqrt{2} \approx 5.657$ for the RD tiling. Hence, one can sample space about 41% more efficiently with an RD grid.

4.3.2 Topology: Thinning Algorithms and Finite Element Methods

Working with TO grids might also simplify 3-D thinning algorithms, since like hexagons in 2-D, there is no neighborhood ambiguity on a TO grid [9]. This could greatly simplify analyses such as those found in [21, 12, 17]. Such neighborhood consistency properties are also desirable in certain finite element modeling applications.

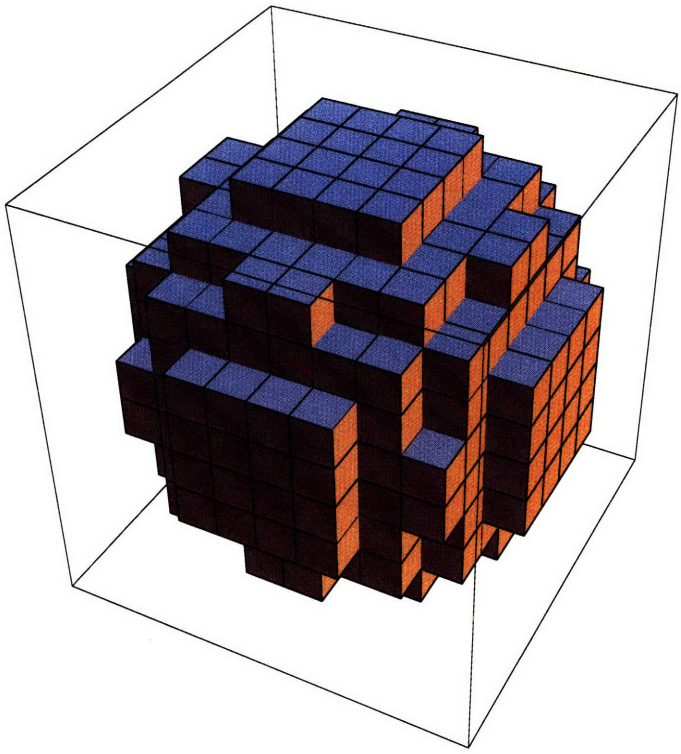

Figure 4-1: A sphere rendered with cubes.

4.3.3 Geometry of Construction

Finally, we consider a few implications of tiling choices in applications where solid voxels are used to conform as closely as possible to a given shape. For example, in creating a foundation using "bricks" of a fixed shape along a boundary whose shape is unknown in advance, the TO grid gives us a smaller surface area boundary than the cubic tiling. As seen from Table 3.1, the TO grid is the winner in this category with a mean area of 1.455 units compared with 1.5 units for that of the cube and the RD. Minimizing exposure to the elements in a construction project by minimizing surface area using this method represents a potential application.

To give the reader a feel for solids which are composed of the various voxels, we include Figures 4-1, 4-2, and 4-3. Minimizing the maximum deviation of a tessellated surface from the original continuous surface which was sampled is another reason one might choose to work with an alternative voxel shape than the cube, which is less spherical than either of the other shapes considered.

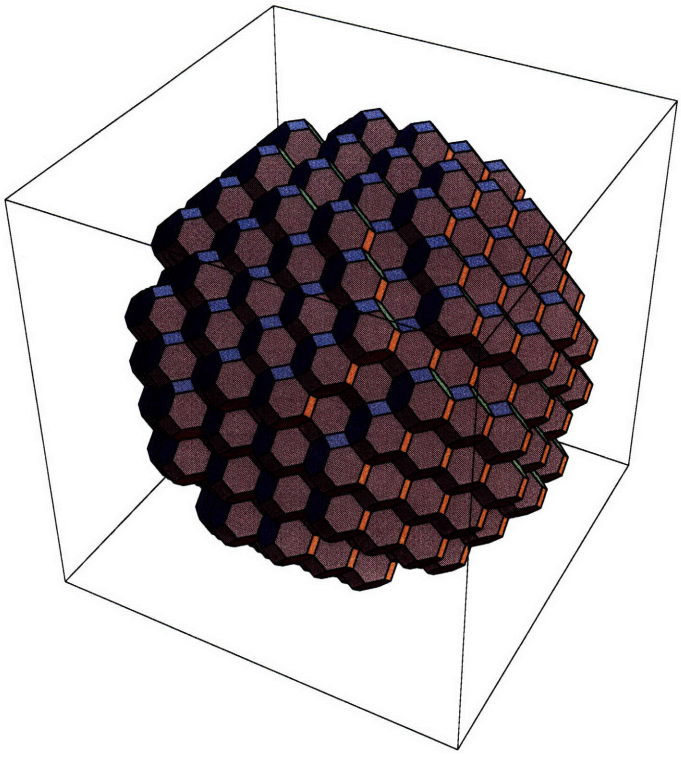

Figure 4-2: A sphere rendered with truncated octahedra.

4.4 Future Work

While we have shown that the rhombic dodecahedron outperforms the truncated octahedron and the cube for the computation of surface area, we have not shown that this is the optimal solid for the job. If we restrict our choices to space-filling parallelohedra (volumes which can fill space through simple parallel displacement), then we must also analyze the triangular prism, the hexagonal prism, and another 14-hedron which tiles space.

As already suggested, random and pseudo-random tilings represent possible interesting solutions to boundary estimate problems, depending on the nature of the problem [11]. Further investigation into these is certainly warranted.

Though this paper focussed on local counting algorithms, there is also potential for the aforementioned tessellations in improving non-local schemes for computing area. Such algorithms may become significantly more efficient or simple when employing these grids rather than the conventional rectangular prism grids.

In summary of our own work once again, we have presented results regarding the

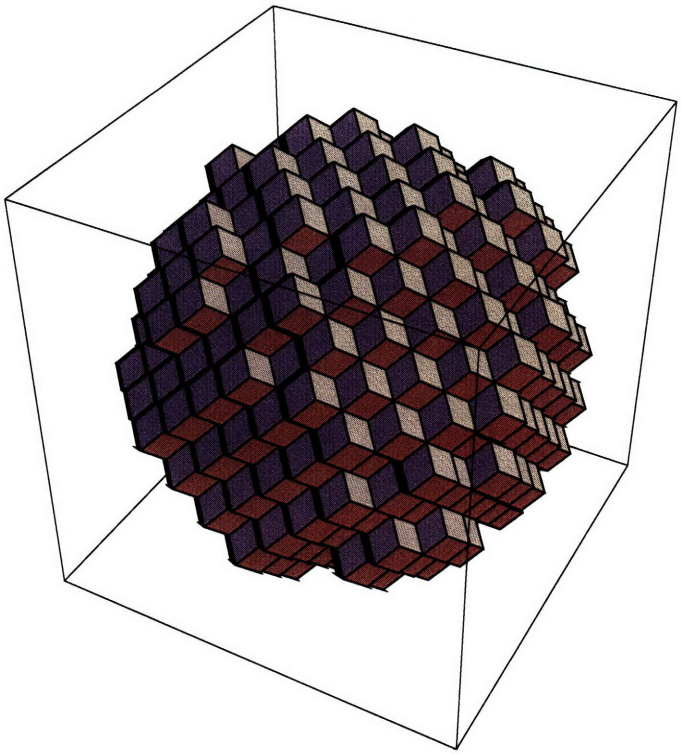

Figure 4-3: A sphere rendered with rhombic dodecahedra.

computation of surface area for arbitrary piecewise smooth binary volumes using local counting algorithms on cubic, truncated octahedral, and rhombic dodecahedral grids.

Appendix A

Tilings

This appendix takes a brief look at some of the possibilities one encounters when choosing a tiling and reviews some of the terminology associated with classes of tilings.

A.1 Tilings

The most familiar tilings of the plane use regular polygons. There are exactly three regular polygons which tile the plane: the equilateral triangle, square, and hexagon [5, page 225]. If we start a tiling by placing the centroid of a polygon over the origin and making one of its edges parallel to the x-axis, then there is a unique tiling for regular hexagons, i.e. they can be arranged in only one way to cover the plane. However, with square and triangular tessellations, rows of tiles can be shifted to give alternate tessellations, such as the "brick wall" tessellation for squares. (Figure A-1D.)

A.1.1 Dirichlet Domains and Dirichlet Tessellations

A *Dirichlet domain* or a *Dirichlet cell* is a set of points, each of which is closer to a given "center" point than to any other "center" point in a group [5, page 225]. (Dirichlet domains in the plane are sometimes called *Voronoi cells.*) An irregular Dirichlet tessellation is shown in Figure A-2. Of the tessellations shown in Figure A-1, only in A and B do the polygons represent Dirichlet domains. In fact, the Dirichlet

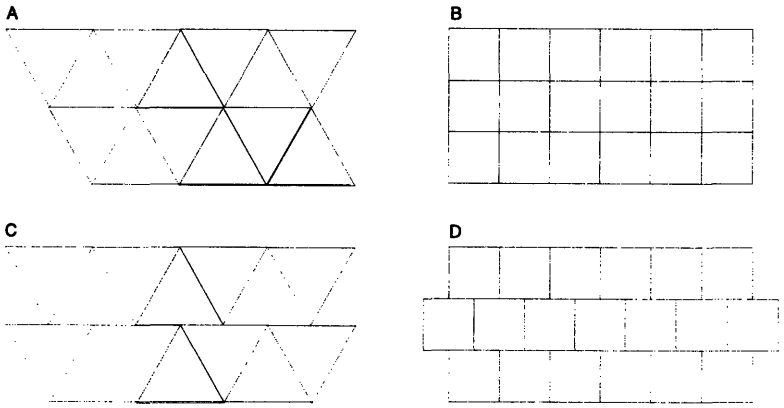

Figure A-1: Square and Triangular Tessellations.

tessellation shown is unique for the square and for the equilateral triangle.[1] As already mentioned, there is only one tessellation by regular hexagons, and this is also a Dirichlet tessellation.

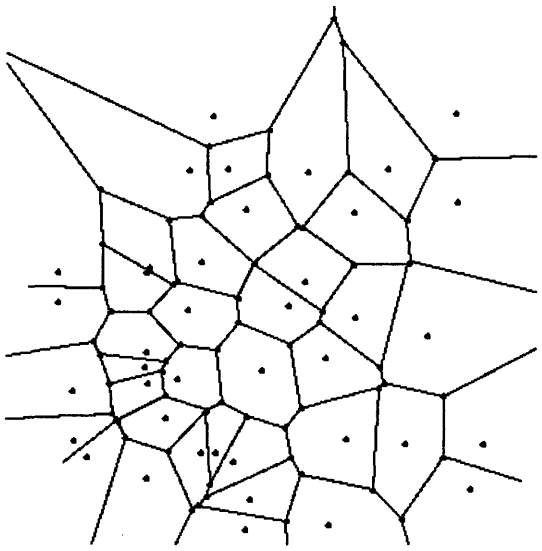

Figure A-2: An irregular Dirichlet Tessellation. Each polygon defines a set of points which are closer to that polygon's "center" point than to any other center point.

[1] A simple constructive proof of this is as follows. Place the first tile at the origin. For the square tessellation, centers of adjacent tiles must lie on the line which is perpendicular to the side of the first square in order to be a Dirichlet tessellation. Hence, there is only one way to place each new tile. By continuing the construction in this manner, there is only one way to tile the plane. Hence the Dirichlet tiling is unique. The same is true for triangular and hexagonal tessellations.

A.1.2 Non-Dirichlet Tessellations

Of the non-Dirichlet tessellations with regular polygons, we define two sub-categories. In the plane, any row of a tessellation (for square and triangular ones) can be translated in one dimension without "breaking" the tessellation. If the relative translation between successive rows of a tessellation is constant, we call it a *shifted tessellation* of angle θ, where θ is the angle formed by the x-axis and the line connecting two corresponding tiles in successive rows. (See Figure A-3.) We conjecture that among shifted tessellations, the tessellation with optimal properties for estimating perimeters of arbitrary shapes is the shifted tessellation of angle 0, that is, the Dirichlet tessellation. 1.4

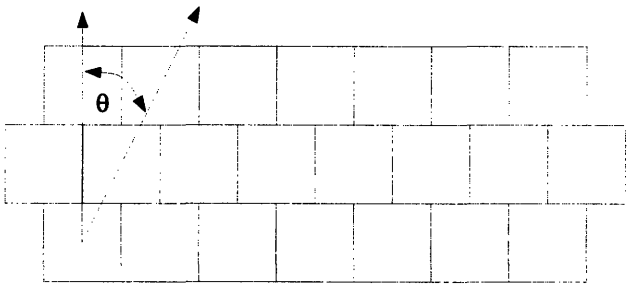

Figure A-3: A shifted square tessellation of angle θ.

There are many other tessellations of interest in computer vision. There are those based on affine transformations of the regular polygonal tessellations (such as rectangular and parallelogram tessellations, obtained simply by shearing the regular polygons). Another interesting set of tilings are those based on stochastic processes. For example, Kulkarni et al. [11] presented some interesting properties of random line tessellations. It is worth keeping in mind the large variety of tessellations and whether any of the others may provide a better domain for the computation of those functions.

Appendix B

Some Identities

The following identities were derived using several equivalences we came across during our analyses. They were used heavily in the derivation of closed form expressions for the area biases for truncated octahedral and rhombic dodecahedral tilings. They are based on two sets of observations, the first having to do with symmetries of certain functions on the unit sphere and the second stemming from different parameterizations of families of planes. Many more such identities could be derived, but these give the basic flavor of the ones which were used in deriving the results in this paper. The main use of these identities was to make difficult integrals easier to solve. In particular, many of the integrals involving the arctan function were simplified in this manner.

B.1 Regions of Symmetry

Recall that the estimated area function for the cube is given by

$$A_C(\theta, \phi) = \sin\phi + \cos\phi\cos\theta + \cos\phi\sin\theta \tag{B.1}$$

Then, by symmetry of coordinates we have the following:

$$\int_0^{\frac{\pi}{4}} \int_0^{\arctan(\cos\theta)} A_C(\theta,\phi)\cos\phi\, d\phi\, d\theta \tag{B.2}$$

$$= \int_{\frac{\pi}{4}}^{\frac{\pi}{2}} \int_0^{\arctan\left(\cos\left(\frac{\pi}{2}-\theta\right)\right)} A_C(\theta,\phi)\cos\phi\, d\phi\, d\theta \tag{B.3}$$

$$= 2 \times \int_0^{\frac{\pi}{4}} \int_{\arctan(\cos\theta)}^{\frac{\pi}{2}} A_C(\theta,\phi)\cos\phi\, d\phi\, d\theta \tag{B.4}$$

$$= 2 \times \int_{\frac{\pi}{4}}^{\frac{\pi}{2}} \int_{\arctan(\cos\theta)}^{\frac{\pi}{2}} A_C(\theta,\phi)\cos\phi\, d\phi\, d\theta \tag{B.5}$$

B.2 Alternative Parameterizations of Planar Segments

A family of planes represented by a lune on the unit sphere (as in Figure 3-2) is described by the range of two parameters, ϕ and θ. Different geometrical interpretations of these parameters (but which represent the same family of planes) give rise to different formulas for computing statistics of these families of planes.

For example, in the case of computing the area bias for cubes, it is useful to consider these parameters to represent the angular deviation of a plane's normal from the z-axis. However, in the case of the rhombic dodecahedron, it is more convenient to consider these angles to be the angles formed between the plane and the x- and y-axes respectively.

These different interpretations lead to multiple expressions for the same quantity, which are expressed in the following identities:

$$\int_0^{\frac{\pi}{4}} \int_0^{\arctan(\cos\theta)} (\cos\phi\cos\theta)\cos\phi\, d\phi\, d\theta \tag{B.6}$$

$$= \int_{\frac{\pi}{4}}^{\frac{\pi}{2}} \int_{0}^{\arctan\left(\cos\left(\frac{\pi}{2}-\theta\right)\right)} (\cos\phi \sin\theta)\cos\phi \, d\phi \, d\theta \tag{B.7}$$

$$= 2 \times \int_{0}^{\frac{\pi}{4}} \int_{\arctan(\cos\theta)}^{\frac{\pi}{2}} (\sin\phi)\cos\phi \, d\phi \, d\theta \tag{B.8}$$

$$= 2 \times \int_{\frac{\pi}{4}}^{\frac{\pi}{2}} \int_{\arctan\left(\cos\left(\frac{\pi}{2}-\theta\right)\right)}^{\frac{\pi}{2}} (\sin\phi)\cos\phi \, d\phi \, d\theta. \tag{B.9}$$

Similarly, we have:

$$\int_{0}^{\frac{\pi}{4}} \int_{0}^{\arctan(\cos\theta)} (\sin\phi)\cos\phi \, d\phi \, d\theta \tag{B.10}$$

$$= \int_{\frac{\pi}{4}}^{\frac{\pi}{2}} \int_{0}^{\arctan\left(\cos\left(\frac{\pi}{2}-\theta\right)\right)} (\sin\phi)\cos\phi \, d\phi \, d\theta \tag{B.11}$$

$$= \int_{\frac{\pi}{4}}^{\frac{\pi}{2}} \int_{0}^{\arctan\left(\cos\left(\frac{\pi}{2}-\theta\right)\right)} (\cos\phi\cos\theta)\cos\phi \, d\phi \, d\theta \tag{B.12}$$

$$= \int_{0}^{\frac{\pi}{4}} \int_{\arctan(\cos\theta)}^{\frac{\pi}{2}} (\cos\phi\cos\theta)\cos\phi \, d\phi \, d\theta$$

$$+ \int_{\frac{\pi}{4}}^{\frac{\pi}{2}} \int_{\arctan\left(\cos\left(\frac{\pi}{2}-\theta\right)\right)}^{\frac{\pi}{2}} (\cos\phi\cos\theta)\cos\phi \, d\phi \, d\theta \tag{B.13}$$

$$= \int_{0}^{\frac{\pi}{4}} \int_{\arctan(\cos\theta)}^{\frac{\pi}{2}} (\cos\phi\sin\theta)\cos\phi \, d\phi \, d\theta$$

$$+ \int_{\frac{\pi}{4}}^{\frac{\pi}{2}} \int_{\arctan\left(\cos\left(\frac{\pi}{2}-\theta\right)\right)}^{\frac{\pi}{2}} (\cos\phi\sin\theta)\cos\phi \, d\phi \, d\theta \tag{B.14}$$

$$= \int_{0}^{\frac{\pi}{4}} \int_{0}^{\arctan(\cos\theta)} (\cos\phi\sin\theta)\cos\phi \, d\phi \, d\theta. \tag{B.15}$$

Appendix C

Derivation of Closed Form Solutions to Mean Estimated Area Integrals

C.1 The Truncated Octahedron Grid

Here we present the derivation of the mean surface area estimates for the truncated octahedron grid. To remind the reader, from Equation 3.14, we have

$$A_T(\phi,\theta) = \left(\frac{1}{4} + \frac{3}{4}\sqrt{3}\right)\sin\phi + \frac{1}{4}\sin\theta\cos\phi + \frac{1}{4}\cos\phi\cos\theta, \quad \{\forall\,(\phi,\theta) \in C\}, \quad \text{(C.1)}$$

as the estimated area formula as a function of the planar segment normals, for planar segments whose normals fall within Region C of Figure 3-2. The integral for mean estimated area is then that shown on the left hand side of Equation 3.15. We compute its value below:

$$\frac{\int\int_C A_T(\phi,\theta)\cos\phi\,d\phi\,d\theta}{\int\int_C \cos\phi\,d\phi\,d\theta} \quad \text{(C.2)}$$

$$= \frac{\int\int_C \left(\left(\frac{1}{4}+\frac{3}{4}\sqrt{3}\right)\sin\phi + \frac{1}{4}\sin\theta\cos\phi + \frac{1}{4}\cos\phi\cos\theta\right)\cos\phi\,d\phi\,d\theta}{\frac{\pi}{6}} \quad \text{(C.3)}$$

$$= \frac{\iint_C \left(\frac{1}{4}\sin\phi+\frac{1}{4}\sin\theta\cos\phi+\frac{1}{4}\cos\phi\cos\theta\right)\cos\phi\,d\phi\,d\theta + \iint_C \left(\frac{3}{4}\sqrt{3}\sin\phi\right)\cos\phi\,d\phi\,d\theta}{\frac{\pi}{6}} \tag{C.4}$$

$$= \frac{\iint_C \frac{1}{4}(\sin\phi+\sin\theta\cos\phi+\cos\phi\cos\theta)\cos\phi\,d\phi\,d\theta + \iint_C \left(\frac{3}{4}\sqrt{3}\sin\phi\right)\cos\phi\,d\phi\,d\theta}{\frac{\pi}{6}} \tag{C.5}$$

$$= \frac{\frac{1}{4}\frac{\pi}{4} + \frac{3\sqrt{3}}{4}\left(\int_0^{\frac{\pi}{4}}\int_{\arctan(\cos\theta)}^{\frac{\pi}{2}}(\sin\phi)\cos\phi\,d\phi\,d\theta + \int_{\frac{\pi}{4}}^{\frac{\pi}{2}}\int_{\arctan\left(\cos\left(\frac{\pi}{2}-\theta\right)\right)}^{\frac{\pi}{2}}(\sin\phi)\cos\phi\,d\phi\,d\theta\right)}{\frac{\pi}{6}} \tag{C.6}$$

$$= \frac{\frac{\pi}{16} + \frac{3\sqrt{3}}{4}\left(2\times\int_0^{\frac{\pi}{4}}\int_{\arctan(\cos\theta)}^{\frac{\pi}{2}}(\sin\phi)\cos\phi\,d\phi\,d\theta\right)}{\frac{\pi}{6}} \tag{C.7}$$

$$= \frac{\frac{\pi}{16} + \frac{3\sqrt{3}}{4}\left(\int_0^{\frac{\pi}{4}}\left(\sin^2\phi\big|_{\arctan(\cos\theta)}^{\frac{\pi}{2}}\right)d\theta\right)}{\frac{\pi}{6}} \tag{C.8}$$

$$= \frac{\frac{\pi}{16} + \frac{3\sqrt{3}}{4}\left(\int_0^{\frac{\pi}{4}}\left(1-\frac{\cos^2\theta}{1+\cos^2\theta}\right)\right)d\theta}{\frac{\pi}{6}} \tag{C.9}$$

$$= \frac{\frac{\pi}{16} + \frac{3\sqrt{3}}{4}\left(\int_0^{\frac{\pi}{4}}\frac{1}{1+\cos^2\theta}\right)d\theta}{\frac{\pi}{6}} \tag{C.10}$$

$$= \frac{\frac{\pi}{16} + \frac{3\sqrt{3}}{4}\left(\frac{\arctan\left(\frac{\tan\theta}{\sqrt{2}}\right)}{\sqrt{2}}\Big|_0^{\frac{\pi}{4}}\right)}{\frac{\pi}{6}} \tag{C.11}$$

$$= \frac{\frac{\pi}{16} + \frac{3\sqrt{6}}{8}\times\arctan\frac{1}{\sqrt{2}}}{\frac{\pi}{6}}. \tag{C.12}$$

Explanations of some of the steps follow. C.4 separates the integral into two parts, one of which is 1/4 of the cubic grid integral we previously computed. This allows us in step C.6 to reduce the left term in the numerator to 1/4 times $\pi/4$. In C.7, we have used the symmetry of the two halves of Region C in Figure 3-2. This could also be inferred from identities B.8 and B.9. The rest of the analysis is just straight forward calculus.

C.2 The Rhombic Dodecahedron Grid

Here we present the derivation of the mean surface area estimates for the rhombic dodecahedron grid. Before proceeding with the body of the derivation, it will be useful to have the following lemma:

$$\int_0^{\frac{\pi}{4}} \left(\arctan\left(\cos\theta\right) + \frac{\cos\theta}{1+\cos^2\theta} \right) \cos\theta \, d\theta = 2\frac{\arctan\frac{1}{\sqrt{2}}}{\sqrt{2}}. \tag{C.13}$$

To prove this we note that

$$2\int_0^{\frac{\pi}{4}} \int_0^{\arctan(\cos\theta)} (\cos\phi\cos\theta)\cos\phi \, d\phi \, d\theta \tag{C.14}$$

$$= 2\int_0^{\frac{\pi}{4}} \int_0^{\arctan(\cos\theta)} \cos^2\phi\cos\theta \, d\phi \, d\theta \tag{C.15}$$

$$= 2\int_0^{\frac{\pi}{4}} \int_0^{\arctan(\cos\theta)} \left(\frac{1+\cos 2\phi}{2}\right)\cos\theta \, d\phi \, d\theta \tag{C.16}$$

$$= \int_0^{\frac{\pi}{4}} \left(\phi + \frac{\sin 2\phi}{2}\right)\cos\theta \Big|_0^{\arctan(\cos\theta)} d\theta \tag{C.17}$$

$$= \int_0^{\frac{\pi}{4}} (\phi + \sin\phi\cos\phi)\cos\theta \Big|_0^{\arctan(\cos\theta)} d\theta \tag{C.18}$$

$$= \int_0^{\frac{\pi}{4}} \left(\arctan\left(\cos\theta\right) + \frac{\cos\theta}{1+\cos^2\theta} \right) \cos\theta \, d\theta, \tag{C.19}$$

which is the left hand side of the lemma, and starting from the same expression we can also produce

$$2\int_0^{\frac{\pi}{4}} \int_0^{\arctan(\cos\theta)} (\cos\phi\cos\theta)\cos\phi \, d\phi \, d\theta \tag{C.20}$$

$$= 2\left(2\int_0^{\frac{\pi}{4}} \int_{\arctan(\cos\theta)}^{\frac{\pi}{2}} (\sin\phi)\cos\phi \, d\phi \, d\theta\right) \tag{C.21}$$

$$= 2\frac{arctan\frac{1}{\sqrt{2}}}{\sqrt{2}}, \tag{C.22}$$

which is the right hand side of the lemma expression. Step C.21 uses Identities B.6 and B.8. Step C.22 duplicates part of the derivation in the immediately preceding derivation for the truncated octahedron, namely, Steps C.7 through C.12. This completes the proof of the lemma.

From Equation 3.17, we have

$$A_R(\phi,\theta) = \sqrt{2}\sin\phi + \frac{1}{2}\cos\phi\cos\left(\theta+\frac{\pi}{4}\right) + \frac{1}{2}\cos\phi\sin\left(\theta+\frac{\pi}{4}\right), \quad \{\forall(\phi,\theta)\in C_L\}, \tag{C.23}$$

as the estimated area formula as a function of the planar segment normals, for planar segments whose normals fall within the left half of Region C of Figure 3-2. The mean estimated area is then

$$\frac{\iint_{C_L} A_R(\phi,\theta)\cos\phi\,d\phi\,d\theta}{\iint_{C_L}\cos\phi\,d\phi\,d\theta} \tag{C.24}$$

$$= \frac{\iint_{C_L}\left(\sqrt{2}\sin\phi+\frac{1}{2}\cos\phi\cos\left(\theta+\frac{\pi}{4}\right)+\frac{1}{2}\cos\phi\sin\left(\theta+\frac{\pi}{4}\right)\right)\cos\phi\,d\phi\,d\theta}{\frac{\pi}{12}} \tag{C.25}$$

$$= \frac{\iint_{C_L}\left(\sqrt{2}\sin\phi+\frac{\sqrt{2}}{2}\cos\phi\cos\theta\right)\cos\phi\,d\phi\,d\theta}{\frac{\pi}{12}} \tag{C.26}$$

$$= \frac{\sqrt{2}\iint_{C_L}(\sin\phi)\cos\phi\,d\phi\,d\theta + \iint_{C_L}\frac{\sqrt{2}}{2}\cos^2\phi\cos\theta\,d\phi\,d\theta}{\frac{\pi}{12}} \tag{C.27}$$

$$= \frac{\sqrt{2}\iint_{C_L}(\sin\phi)\cos\phi\,d\phi\,d\theta + \frac{\sqrt{2}}{4}\iint_{C_L}(1+\cos 2\phi)\cos\theta\,d\phi\,d\theta}{\frac{\pi}{12}} \tag{C.28}$$

$$= \frac{\sqrt{2}\frac{\arctan\left(\frac{1}{\sqrt{2}}\right)}{2\sqrt{2}} + \frac{\sqrt{2}}{4}\int_0^{\frac{\pi}{4}}\left(\phi+\frac{\sin 2\phi}{2}\right)\Big|_{\arctan(\cos\theta)}^{\frac{\pi}{2}}\cos\theta\,d\theta}{\frac{\pi}{12}} \tag{C.29}$$

$$= \frac{\frac{\arctan\left(\frac{1}{\sqrt{2}}\right)}{2} + \frac{\sqrt{2}}{4}\int_0^{\frac{\pi}{4}}\left(\frac{\pi}{2}-\left(\arctan(\cos\theta)+\frac{\sin(2\arctan(\cos\theta))}{2}\right)\right)\cos\theta\,d\theta}{\frac{\pi}{12}} \tag{C.30}$$

$$= \frac{\frac{\arctan\left(\frac{1}{\sqrt{2}}\right)}{2}}{\frac{\pi}{12}} + \tag{C.31}$$

$$\frac{\frac{\sqrt{2}}{4}\int_0^{\frac{\pi}{4}}\left(\frac{\pi}{2}-(\arctan(\cos\theta)+\sin(\arctan(\cos\theta))\cos(\arctan(\cos\theta)))\right)\cos\theta d\theta}{\frac{\pi}{12}} \tag{C.31}$$

$$= \frac{\frac{\arctan\left(\frac{1}{\sqrt{2}}\right)}{2}+\frac{\sqrt{2}}{4}\int_0^{\frac{\pi}{4}}\left(\frac{\pi}{2}-\left(\arctan(\cos\theta)+\frac{\cos\theta}{1+\cos^2\theta}\right)\right)\cos\theta\, d\theta}{\frac{\pi}{12}} \tag{C.32}$$

$$= \frac{\frac{\arctan\left(\frac{1}{\sqrt{2}}\right)}{2}+\frac{\sqrt{2}}{4}\left(\int_0^{\frac{\pi}{4}}\frac{\pi}{2}\cos\theta\, d\theta-\int_0^{\frac{\pi}{4}}\left(\arctan(\cos\theta)+\frac{\cos\theta}{1+\cos^2\theta}\right)\cos\theta\, d\theta\right)}{\frac{\pi}{12}} \tag{C.33}$$

$$= \frac{\frac{\arctan\left(\frac{1}{\sqrt{2}}\right)}{2}+\frac{\sqrt{2}}{4}\left(\int_0^{\frac{\pi}{4}}\frac{\pi}{2}\cos\theta\, d\theta-2\frac{\arctan\frac{1}{\sqrt{2}}}{\sqrt{2}}\right)}{\frac{\pi}{12}} \tag{C.34}$$

$$= \frac{\frac{\arctan\left(\frac{1}{\sqrt{2}}\right)}{2}+\frac{\sqrt{2}}{4}\left(\frac{\pi}{2}\frac{\sqrt{2}}{2}-2\frac{\arctan\frac{1}{\sqrt{2}}}{\sqrt{2}}\right)}{\frac{\pi}{12}} \tag{C.35}$$

$$= \frac{\frac{\arctan\left(\frac{1}{\sqrt{2}}\right)}{2}+\frac{\pi}{8}-\frac{\arctan\left(\frac{1}{\sqrt{2}}\right)}{2}}{\frac{\pi}{12}} \tag{C.36}$$

$$= \frac{3}{2}. \tag{C.37}$$

Well that was a lot of work to get an answer of 3/2! Explanations of some of the steps are below. C.25 uses the standard sum of angles identity. C.28 uses the results from the TO derivation to produce the arctan expression of the leftmost term in C.29. C.30 applies the double angle identity for sin. Finally, C.33 uses the lemma proved above to simplify the nasty integral.

Appendix D

Tiling a Planar Patch: Some Additional Figures

This appendix provides some additional figures which may elucidate some of the derivations in the text. In the first section, we examine the three primary projections of a planar patch represented with truncated octahedra. In the second section, we do the same for rhombic dodecahedra.

D.1 The Truncated Octahedron Projections

Figure D-1 shows a planar patch represented with truncated octahedra.

Figure D-2 shows this same patch projected onto the x-y plane, with a slight adjustment in the point of view. By skewing the point of view slightly, the voxels which get hidden by the projection can be visualized.

In Figure D-3, we project onto the x-z plane. Again, we adjust the point of view slightly away from a straight projection to give perspective and show the organization of the surface.

Figure D-4 shows the projection onto the y-z plane. Notice that there are no "hidden" voxels for this projection, only hidden facets. That is, the projection contains a part of every voxel which contributes to the surface area of the tessellated planar patch.

Figure D-5 shows all of the images together for comparison.

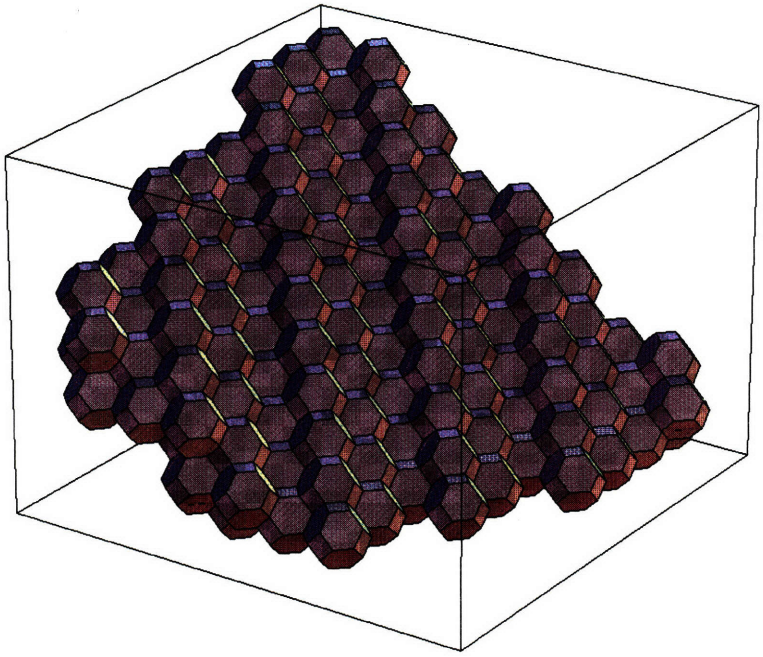

Figure D-1: A planar patch represented with truncated octahedra.

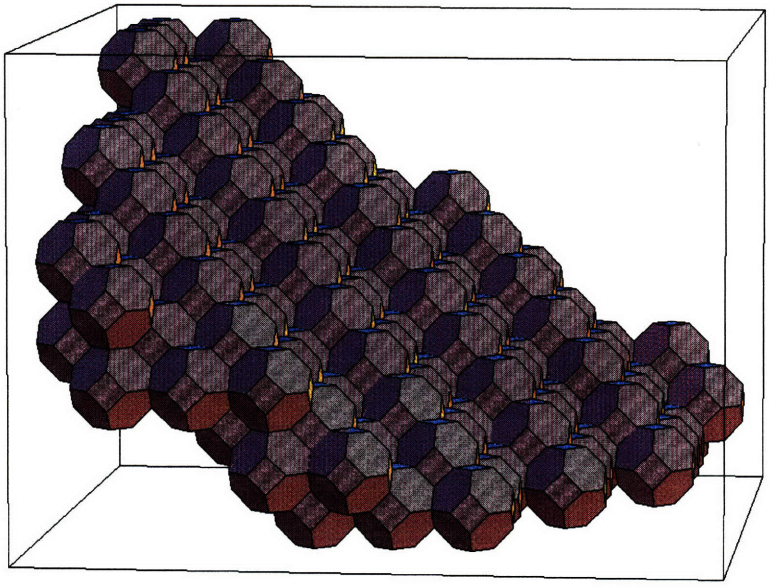

Figure D-2: The projection of the planar patch onto the x-y plane.

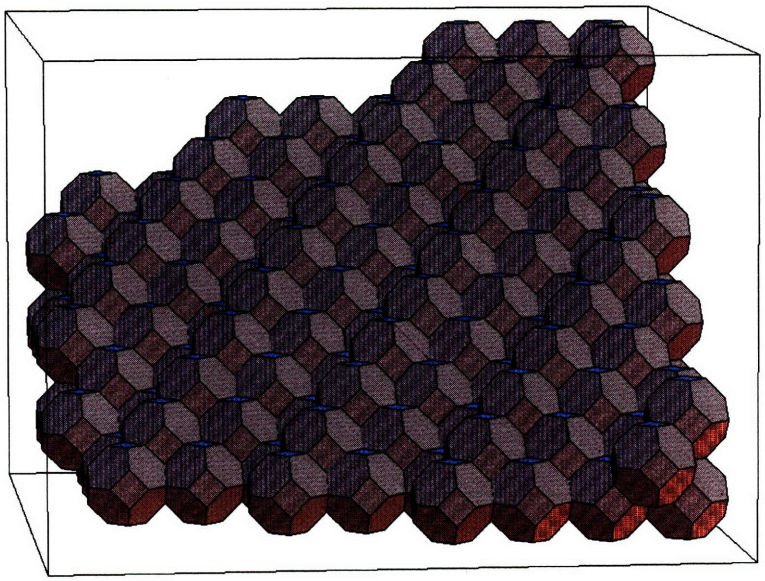

Figure D-3: The projection of the planar patch onto the x-z plane.

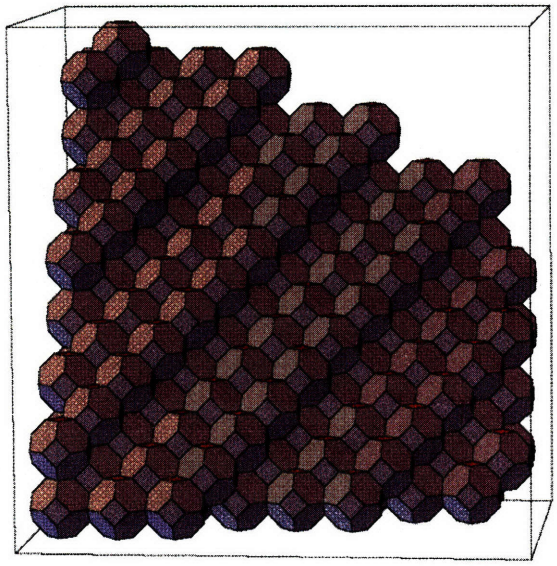

Figure D-4: The projection of the planar patch onto the y-z plane.

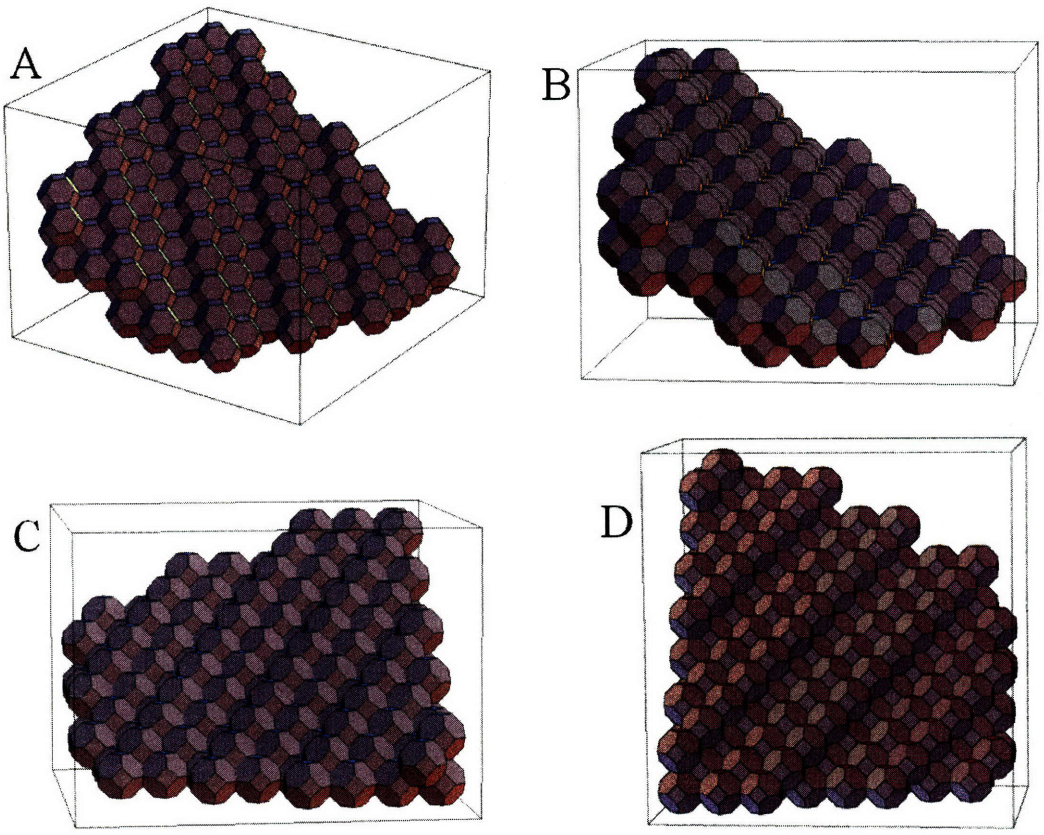

Figure D-5: The oblique view of a planar patch (A) along with its three major projections (B, C, D).

D.2 The Rhombic Dodecahedron Projections

The sequence of figures in this section parallels the progression in the previous section. Figure D-6 is a plane tessellated with rhombic dodecahedra. Figures D-7, D-8, and D-9 are the three major projections of that plane from slightly skewed viewpoints. And finally, Figure D-10 is a composite of the four images.

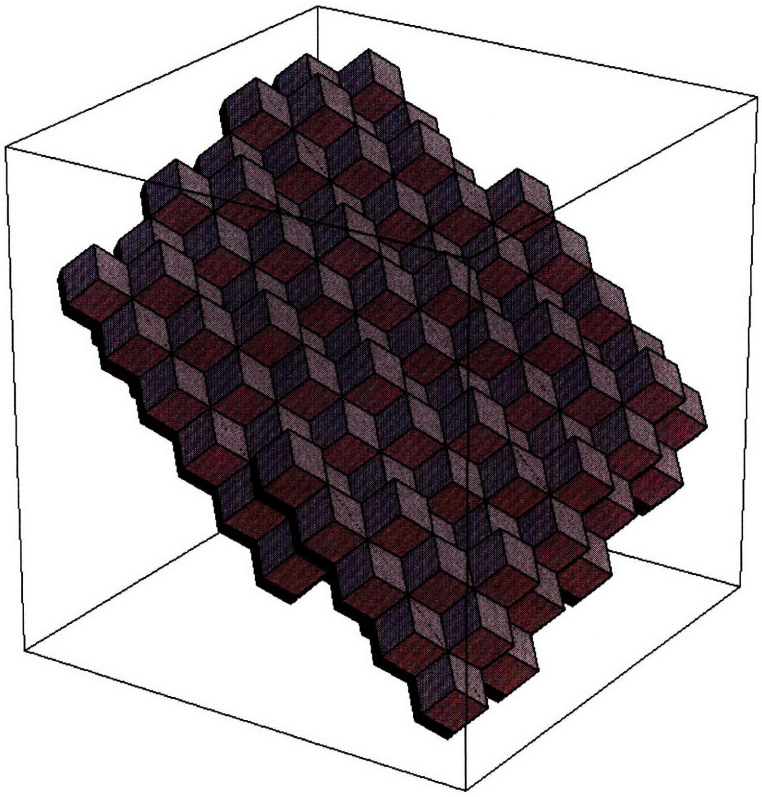

Figure D-6: A planar patch represented with rhombic dodecahedra.

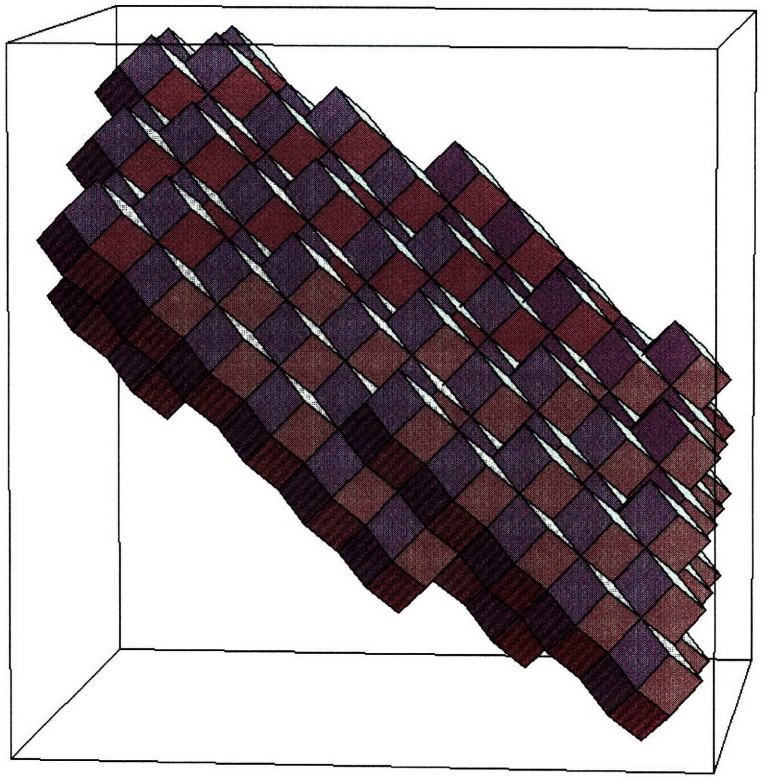

Figure D-7: The projection of the planar patch onto the x-y plane.

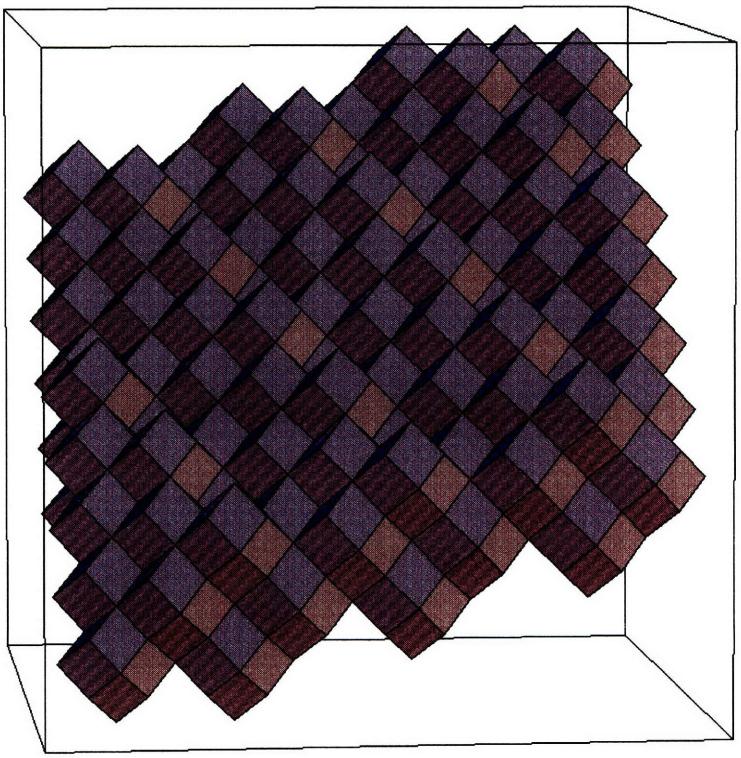

Figure D-8: The projection of the planar patch onto the x-z plane.

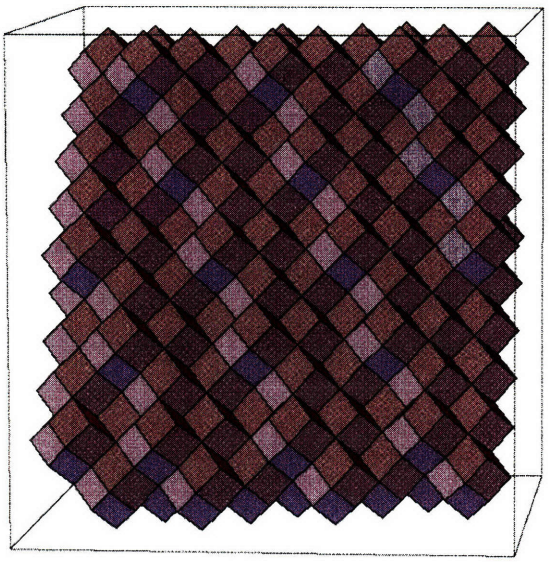

Figure D-9: The projection of the planar patch onto the y-z plane.

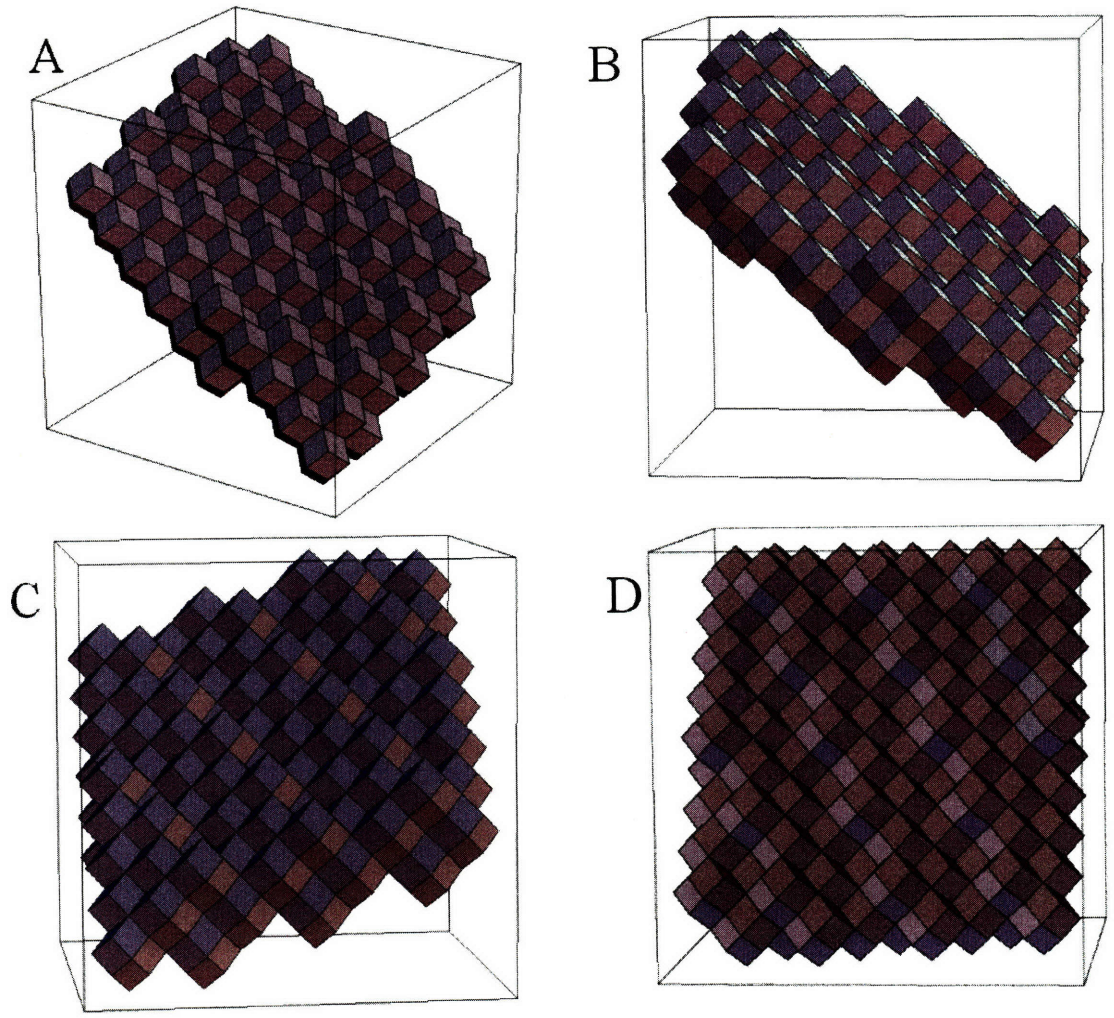

Figure D-10: The oblique view of a planar patch (A) along with its three major projections (B, C, D).

Bibliography

[1] Nadim M. Aziz and Sudarshan P. Bhat. On the computation of integral properties of objects. *Advances in Engineering Software*, 12(4):174–180, 1990.

[2] E. S. Deutsch. Thinning algorithms on rectangular, hexagonal, and triangular arrays. *Communications of the ACM*, 15:827–837, 1972.

[3] Eric Dubois. The sampling and reconstruction of time-varying imagery with application in video systems. *Proceedings of the IEEE*, 73(4):502–522, 1985.

[4] James Foley, Andries van Dam, Steven Feiner, and John Hughes. *Computer Graphics: Principles and Practice, 2nd Edition.* Addison-Wesley, Reading, Massachusetts, 1992.

[5] Peter C. Gasson. *Geometry of Spatial Forms: Analysis, Synthesis, Concept Formulation and Space Vision for CAD.* Ellis Horwood Limited, Chicester, England, 1983.

[6] M. J. E. Golay. Hexagonal parallel pattern transformations. *IEEE Transactions on Computers*, pages 733–740, 1969.

[7] S. B. Gray. Local properties of binary images in two dimensions. *IEEE Transactions on Computers*, pages 551–561, 1971.

[8] Innchyn Her and Chi-Tseng Yuan. Resampling on a pseudohexagonal grid. *CVGIP: Graphical Models and Image Processing*, 56(4):336–347, 1994.

[9] Berthold K. P. Horn. *Robot Vision.* MIT Press, Cambridge, Massachusetts, 1986.

[10] Jack Koplowitz and Alfred M. Bruckstein. Design of perimeter estimators for digitized planar shapes. *IEEE Transactions of Pattern Analysis and Machine Intelligence*, 11:611–622, 1989.

[11] Sanjeev R. Kulkarni, Sanjoy K. Mitter, T. J. Richardson, and John N. Tsitsiklis. Local versus nonlocal computation of length in digitized curves. *IEEE Transactions on Pattern Analysis and Machine Intelligence*, 16:711–718, 1994.

[12] Chung-Nim Lee, Timothy Poston, and Azriel Rosenfeld. Winding and Euler numbers for 2D and 3D digital images. *CVGIP: Image Understanding*, 53(6):522–537, 1991.

[13] Yong Tsui Lee and Aristides A. G. Requicha. Algorithms for computing the volume and other integral properties of solids. I. Known methods and open issues. *Communications of the ACM*, 25(9):635–641, 1982.

[14] Yong Tsui Lee and Aristides A. G. Requicha. Algorithms for computing the volume and other integral properties of solids. II. A family of algorithms based on representation conversion and cellular approximation. *Communications of the ACM*, 25(9):642–650, 1982.

[15] Ed Luczak and Azriel Rosenfeld. Distance on a hexagonal grid. *IEEE Transactions On Computers*, pages 523–533, May 1976.

[16] L. A. Lyusternik. *Convex Figures and Polyhedra.* Dover, New York, New York, 1963.

[17] Cherng Min Ma. On topology preservation in 3D thinning. *CVGIP: Image Understanding*, 59(3):328–339, 1994.

[18] Greg McCarthy and Marie Luby. Imaging the structural changes associated with human epilepsy. *Clinical Neuroscience*, 2:82–88, 1994.

[19] Russell M. Mersereau. The processing of hexagonally sampled two-dimensional signals. *Proceedings of the IEEE*, 67(6):930–949, 1979.

[20] R. G. Petty, G. Pearlson, I. McGilchrist, R. Lewis, A. Y. Tien, A. Pulver, D. D. Vaughn, M. F. Casanova, R. E. Powers, and P. E. Barta. Reversal of asymmetry of the planum temporale in schizophrenia. *American Journal of Psychiatry*, 152:715–721, 1995.

[21] P. K. Saha and B. B. Chaudhuri. 3D digital topology under binary transformation with applications. *Computer Vision and Image Understanding*, 63:418–429, 1996.

[22] Luis A. Santalo. *Integral Geometry and Geometric Proabability.* Addison-Wesley, Reading, Massachusetts, 1976.

[23] Herbert Solomon. *Geometric Probability.* Society for Industrial and Applied Mathematics, Philadelphia, Pennsylvania, 1978.

[24] Eric W. Weisstein. Eric's treasure trove of mathematics. *World Wide Web Document: http://astsun.astro.virginia.edu/~ eww6n/math/*, 1997.

[25] Stephen Wolfram. *The Mathematica Book, 3rd Edition.* Wolfram Media, Champaign, Illinois, 1996.